**Frontiers in Heat and Mass Transfer**

Available at www.ThermalFluidsCentral.org

# FUNDAMENTALS AND APPLICATIONS OF NEAR-FIELD RADIATIVE ENERGY TRANSFER

Keunhan Park[a,*] and Zhuomin Zhang[b]

[a]*Department of Mechanical, Industrial and Systems Engineering, University of Rhode Island, Kingston, RI 02881, USA*
[b]*G.W. Woodruff School of Mechanical Engineering, Georgia Institute of Technology, Atlanta, GA 30332-0405, USA*

**ABSTRACT**

This article reviews the recent advances in near-field radiative energy transfer, particularly in its fundamentals and applications. When the geometrical features of radiating objects or their separating distances fall into the sub-wavelength range, near-field phenomena such as photon tunneling and surface polaritons begin to play a key role in energy transfer. The resulting heat transfer rate can greatly exceed the blackbody radiation limit by several orders magnitude. This astonishing feature cannot be conveyed by the conventional theory of thermal radiation, generating strong demands in fundamental research that can address thermal radiation in the near field. Important breakthroughs of near-field thermal radiation are presented here, covering from the essential physics that will help better understand the basics of near-field thermal radiation to the most recent theoretical as well as experimental findings that will further promote the fundamental understanding. Applications of near-field thermal radiation in various fields are also discussed, including the radiative property manipulation, near-field thermophotovoltaics, nanoinstrumentation and nanomanufacturing, and thermal rectification.

**Keywords**: *thermal radiation, micro/nanoscale, radiative properties, thermophotovoltaics, nanoinstrumentation, nanomanufacturing*

## 1. INTRODUCTION

Conventionally, the theory of thermal radiation is based on the concept of blackbody, cast by Gustav Kirchhoff in 1860. A blackbody absorbs all energy of the radiation rays reaching it geometrically. Among all objects at the same temperature with the same geometry, a blackbody emits the largest amount of energy when measured in the same angular and spectral ranges. As such, the Stefan-Boltzmann law and Planck's law provide descriptions of the total and spectral characteristics of blackbodies. Thermal emission from real materials can be described by comparison with that emitted by a blackbody at the same temperature using a property called emissivity (also called emittance). Although care should be taken with regards to the proper definition of emissivity (spectral, total, directional, individual polarization versus polarization averaged, etc.) (Howell *et al.*, 2010; Modest, 2003; Zhang, 2007), the emissivity should be always smaller than unity in conventional thermal radiation: that is, thermal emission from real materials is always smaller than that from the blackbody in the far-field regime.

Conventional radiative transfer approaches are often not applicable when the geometric features or distances are smaller than the characteristic wavelength of thermal radiation based on the Wien's displacement law (Zhang and Wang, 2012). Planck (1914) noted that the spectral distribution of blackbody radiation is derived based on the assumption that the geometric dimensions of the enclosure (also called a blackbody cavity) are much greater than the characteristic wavelength of thermal radiation. This condition makes Planck's law only applicable in the far

field, i.e., away from the surface of any objects. In essence, thermal radiation can be understood as electromagnetic (EM) waves emitted due to the random fluctuation of charges in the material. When a material is in thermal equilibrium at temperature $T$, charges such as free electrons (for metals) or ions (for polar materials) experience a random thermal motion and radiate the fluctuating EM field. While the average of the fluctuating electric or magnetic field is zero due to its random nature, the energy density and Poynting vector (which characterizes the energy flux) are nonzero and can greatly exceed the blackbody radiation depending on the dielectric and magnetic properties of materials (Rytov *et al.*, 1987). In particular, evanescent EM fields near the interface, which do not carry energy alone and exponentially decay from the interface, are coupled to carry a significant portion of energy across the gap when two objects are placed closer than the characteristic wavelength of thermal radiation. This phenomenon is known as photon tunneling and is responsible for the enhanced energy transfer in the near field, along with other near-field effects such as interference and surface polaritons (Zhang, 2007; Fu and Zhang, 2006; Basu *et al.*, 2009). Such near-field effects can also alter the far-field properties of nanostructured surfaces or objects. In the far-field, no matter how complex the structure is, the emissivity and transmittance cannot exceed unity. However, unique spectral- and angular-dependent radiative properties can be achieved by engineering nano/microstructures (Zhang and Wang, 2011). Surface waves and photonic band structures are often utilized to enable unique optical properties of nano/microstructures

---

*Corresponding author. Email: kpark@egr.uri.edu*

(Fu and Zhang, 2009).

Near-field radiation holds promise for applications in energy systems, nanofabrication and near-field imaging. Rapidly depleting reserves of fossil fuels and the concern of the global warming have placed a great demand of alternative power generation technologies. One of such technology is a thermophotovoltaic (TPV) system, which operates on the principle similar to that of solar cells (but with a lower bandgap) to generate electricity from thermal emission. A possible method of improving the performance of TPV systems is to employ near-field thermal radiation for the energy conversion (Basu *et al.*, 2007). However, large near-field thermal radiation is not always favorable in some energy conversion systems: as revealed by Dillner (2008), near-field thermal radiation needs to be suppressed to increase the thermoelectric energy conversion efficiency of thermotunneling devices. Besides the energy conversion, near-field thermal radiation has also been used for imaging beyond the diffraction limit (De Wilde *et al.*, 2006; Kittel *et al.*, 2005). Furthermore, the concept of using near-field radiation as thermal rectifier has also been suggested (Otey *et al.*, 2010; Basu and Francoeur, 2011a). Limiting the magnitude of near-field radiation is critical for improving the performance of thermal tunneling devices (Dillner, 2008). Another important application of near-field radiation is in the field of nanomanufacturing. Enhanced transmission of metallic films perforated with subwavelength holes stirred the interest in studying light transmission through nanostructures. Nanolithography techniques based on the surface plasmon waves have been demonstrated for patterning structures of less than 50 nm (Liu *et al.*, 2005; Wang *et al.*, 2006). Furthermore, nanoscale direct writing has also been demonstrated using near-field optics coupled with femtosecond laser (Grigoropoulos *et al.*, 2007).

This review article provides a thorough review of near-field thermal radiation, covering the essential physics of fluctuational electromagnetism along with recent advances in fundamentals and applications of near-field thermal radiation. The remaining sections are organized as follows. Section 2 focuses on the essential physics of near-field thermal radiation by introducing the fluctuation-dissipation theorem, Dyadic Green's function, dielectric functions, and surface polaritons. Recent advances on the fundamental research of near-field thermal radiation are discussed in the following sections. Starting from near-field radiative heat transfer between two semi-infinite media, Section 3 discusses the upper limit of near-field radiative heat flux and the extremely small penetration depth of near-field thermal radiation, as well as energy streamlines – a novel way to elucidate the near-field energy propagation between semi-infinite media and multilayered structures. Near-field thermal radiation in other geometries, such as sphere-sphere and sphere-flat surface, and between emerging nanomaterials is covered in Section 4, followed by the discussion of experimental observations of near-field radiative heat transfer in Section 5. Section 6 looks into the applications of near-field thermal radiation, including the manipulation of radiative properties, near-field thermophotovoltaics, tip-based engineering, and thermal rectification. In conclusion, a brief summary on the recent progresses in fundamentally understanding and engineering near-field thermal radiation is provided along with remarks on future research opportunities and challenges of the field.

## 2. ESSENTIAL PHYSICS OF NEAR-FIELD THERMAL RADIATION

### 2.1. Fluctuation-Dissipation Theorem

Thermal radiation between solids is traditionally treated as a surface phenomenon with the concept of emissivity, reflectivity and absorptivity of the surfaces. Radiation heat transfer in a participating medium is thus analyzed using ray optics, leading to the development of the radiative transfer equation (RTE) that considers emission, absorption, and scattering of thermally emitted rays in the medium (Howell *et al.*,

2010). Although RTE can determine the radiation distribution within the medium by computing the intensity along the propagation of radiation, this phenomenological equation does not fully account for the fundamentals of thermal emission and breaks down when wave interference and diffraction become important. To speculate the origin of thermal radiation, Rytov and his co-workers (1987) combined the fluctuation-dissipation theorem and Maxwell's equations to establish the fluctuational electrodynamics. According to the fluctuation-dissipation theorem, thermal radiation is essentially EM waves emitted from the fluctuating currents due to the random thermal motion of charges, known as thermally induced dipoles, in a medium. Thus the propagation of thermal radiation and its interaction with matter can be fully described in the framework of the fluctuational electrodynamics, in both the far-field and near-field regimes.

When a material is in thermal equilibrium at temperature $T$, charges in the material – electrons in metals or ions in polar crystals – are subject to random thermal motions and generate fluctuating electric currents. The fluctuating electric density $\mathbf{j}(\mathbf{x},t)$, or $\mathbf{j}(\mathbf{x},\omega)$ in the frequency domain, can be implemented in Maxwell's equations as an external source to make the equations stochastic. The key issue in calculating thermally induced, fluctuating EM waves is then how to determine the statistical properties of these random sources. According to the fluctuation-dissipation theorem (FDT), while the fluctuating electric density is averaged to zero (i.e., $\langle j_m(\mathbf{x},\omega) \rangle = 0$) due to its random nature, the ensemble average of its cross-spectral spatial correlation function is nonzero and expressed as (Joulain *et al.*, 2005):

$$\langle j_m(\mathbf{x}',\omega) j_n^*(\mathbf{x}'',\omega') \rangle =$$
$$\frac{4}{\pi} \omega \varepsilon_0 \mathrm{Im}(\varepsilon(\omega)) \delta_{mn} \delta(\mathbf{x}' - \mathbf{x}'') \Theta(\omega, T) \delta(\omega - \omega') \quad (1)$$

where $\langle \ \rangle$ represents ensemble averaging, and $*$ denotes the complex conjugate. In Eq. (1), $\varepsilon_0$ is the electrical permittivity of the free space, $j_m$ and $j_n$ ($m, n = 1, 2,$ or $3$) stands for the $x$, $y$, or $z$ component of $\mathbf{j}$, $\delta_{mn}$ is the Kronecker delta, and $\delta(\mathbf{x}' - \mathbf{x}'')$ and $\delta(\omega - \omega')$ are the Dirac delta function. $\Theta(\omega, T)$ is the mean energy of a Planck oscillator at the frequency $\omega$ in thermal equilibrium at temperature $T$ and is given by $\Theta(\omega, T) = \hbar\omega / [exp(\hbar\omega/k_{\mathrm{B}}T) - 1]$, where $\hbar$ is the Planck constant divided by $2\pi$ and $k_{\mathrm{B}}$ is the Boltzmann constant. Since only positive values of frequencies are considered here, a factor of 4 has been included in Eq. (1) to consistently use the conventional definitions of the spectral energy density and the Poynting vector (Fu and Zhang, 2006).

### 2.2. Dyadic Green's Function

For prescribed geometric conditions and temperature, Maxwell's equations need to be solved in order to obtain the electric and magnetic field distributions. This can be done with the help of the dyadic Green's function, which makes the formulations simple and compact. With the assistance of the dyadic Green's function $\overline{\overline{\mathbf{G}}}_e(\mathbf{x}, \mathbf{x}', \omega)$, the induced electric and magnetic fields due to the fluctuating current density can be expressed respectively in the frequency domain as volume integrations:

$$\mathbf{E}(\mathbf{x}, \omega) = i\omega\mu_0 \int_V \overline{\overline{\mathbf{G}}}_e(\mathbf{x}, \mathbf{x}', \omega) \cdot \mathbf{j}(\mathbf{x}', \omega) d\mathbf{x}' \quad (2)$$

$$\mathbf{H}(\mathbf{x}, \omega) = \int_V \overline{\overline{\mathbf{G}}}_h(\mathbf{x}, \mathbf{x}', \omega) \cdot \mathbf{j}(\mathbf{x}', \omega) d\mathbf{x}' \quad (3)$$

where $\overline{\overline{\mathbf{G}}}_h(\mathbf{x}, \mathbf{x}', \omega) = \nabla \times \overline{\overline{\mathbf{G}}}_e(\mathbf{x}, \mathbf{x}', \omega)$ is the magnetic dyadic Green's function, $\mu_0$ is the magnetic permeability of vacuum, and the integral is over the region V that contains the fluctuating sources. The dyadic Green's function, $\overline{\overline{\mathbf{G}}}_e(\mathbf{x}, \mathbf{x}', \omega)$ is essentially a spatial transfer function between a point source at location $\mathbf{x}'$ and the resultant electric field $\mathbf{E}$ at $\mathbf{x}$ (Zhang, 2007). Based on the ergodic hypothesis, the spectral energy
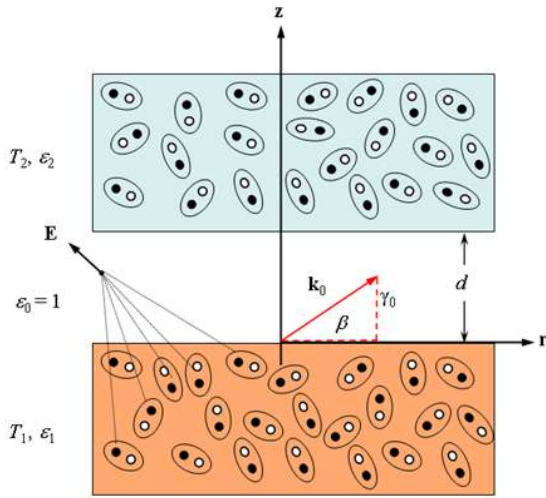
**Fig. 1** Schematic of near-field radiative heat transfer between two closely spaced semi-infinite plates, at temperatures $T_1$ and $T_2$, separated by a vacuum gap $d$.



**Fig. 2** Schematic of a multilayered thin-film structure for Green's function analysis. Each of the films may be at a different temperature.

flux is given by (Basu *et al.*, 2009)

$$\langle \mathbf{S}(\mathbf{x}, \omega) \rangle = \int_0^\infty \frac{1}{2} \left\langle \mathrm{Re}[\mathbf{E}(\mathbf{x}, \omega') \times \mathbf{H}^*(\mathbf{x}, \omega')] \right\rangle d\omega' \quad (4)$$

where $\mathbf{S}$ is the spectral Poynting vector, $\omega$ (and $\omega'$) is the angular frequency. In order to compute the spectral Poynting vector at $\mathbf{x}$, we should compute the cross-spectral density of electric and magnetic field vectors $E_i(\mathbf{x}, \omega)$ and $H_j(\mathbf{x}, \omega')$ . The cross-spectral density can be written as

$$\langle E_i(\mathbf{x}, \omega) H_j^*(\mathbf{x}, \omega') \rangle = i\omega\mu_0 \int_V d\mathbf{x}' \int_V d\mathbf{x}''$$
$$\left\{ G_{e,im}(\mathbf{x}, \mathbf{x}', \omega) G_{h,jn}(\mathbf{x}, \mathbf{x}'', \omega') \langle j_m(\mathbf{x}', \omega) j_n^*(\mathbf{x}'', \omega') \rangle \right\} \quad (5)$$

With the relationship between the fluctuating current densities and the temperature of the emitting medium being established through Eq. (1), the spectral radiative heat flux can be calculated using Eq. (5) once the dyadic electric Green's function, $\overline{\overline{\mathbf{G}}}_e(\mathbf{x}, \mathbf{x}', \omega)$ is obtained. Since the dyadic Green's function depends on the geometry of the physical system, the following sections will briefly describe the dyadic Green's functions for two representative structures, i.e., for two semi-infinite media and multilayered media.

**Two semi-infinite media:** Let's consider near-field thermal radiation between two semi-infinite media separated by a vacuum gap (or a dielectric medium) of width $d$, when they are in thermal equilibrium at temperatures $T_1$ and $T_2$, respectively, where $T_1 > T_2$. Both media are nonmagnetic, isotropic, and homogeneous, and surfaces are parallel and smooth. As illustrated in Fig. 1, dipoles in the media are in random motions, radiating space-time dependent fluctuating electric field, $\mathbf{E}(\mathbf{x}, t)$. Cylindrical coordinate system is used so that the space variable $\mathbf{x} = \mathbf{r} + \mathbf{z}$, with $r$-direction being parallel to the interface and $z$-direction perpendicular to the interface. $\beta$ and $\gamma_j$ refer to the $r$-component and $z$-component of the wavevector $\mathbf{k}_j$, respectively. Thus, $\mathbf{k}_j = \beta\hat{\mathbf{r}} + \gamma_j\hat{\mathbf{z}}$ and $k_j^2 = \beta^2 + \gamma_j^2$, for $j = 0$, 1, and 2. The magnitude of $\mathbf{k}_j$ is related to the dielectric function $\varepsilon_j$ by $k_0 = \omega/c$, $k_1 = \sqrt{\varepsilon_1}\omega/c$, and $k_2 = \sqrt{\varepsilon_2}\omega/c$, with $c$ being the speed of light in vacuum and $\varepsilon_1$ and $\varepsilon_2$ being the dielectric functions (or relative permittivity) of medium 1 and 2, respectively. For the described two semi-infinite media, the dyadic Green's function takes the following form (Fu and Zhang, 2006; Joulain
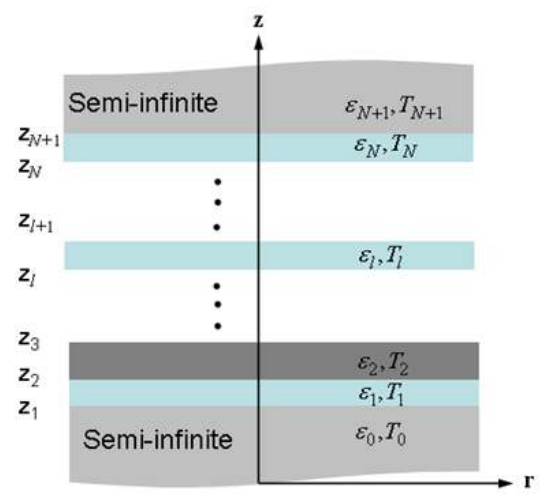
*et al.*, 2005)

$$\overline{\overline{\mathbf{G}}}_e(\mathbf{x}, \mathbf{x}', \omega) =$$
$$\int_0^\infty \frac{i}{4\pi\gamma_1} \left( \hat{\mathbf{s}} t_{12}^{\mathrm{s}} \hat{\mathbf{s}} + \hat{\mathbf{p}}_2 t_{12}^{\mathrm{p}} \hat{\mathbf{p}}_1 \right) e^{i(\gamma_2 z - \gamma_1 z')} e^{i\beta(r-r')} \beta d\beta \quad (6)$$

where $\mathbf{x} = r\hat{\mathbf{r}} + z\hat{\mathbf{z}}$ and $\mathbf{x}' = r'\hat{\mathbf{r}} + z'\hat{\mathbf{z}}$. The unit vectors are $\hat{\mathbf{s}} = \hat{\mathbf{r}} \times \hat{\mathbf{z}}$ and $\hat{\mathbf{p}}_{1(2)} = \left( \beta\hat{\mathbf{z}} - \gamma_{1(2)}\hat{\mathbf{r}} \right)/k_1$. Note that $t_{12}^{\mathrm{s}}$ and $t_{12}^{\mathrm{p}}$ are the transmission coefficients from medium 1 to medium 2 for $s$- and $p$-polarizations, respectively, given by Airy's formula (Zhang, 2007). Provided that $t_{12}^{\mathrm{s}}$ and $t_{12}^{\mathrm{p}}$ take into account multiple reflections in the vacuum layer, the dyadic Green's function describes the transfer of the electromagnetic fields through propagating waves (i.e., $\beta < k_j$) and evanescent waves (i.e., $\beta > k_j$), from a point source at $\mathbf{x}'$ to a receiving point at $\mathbf{x}$.

**Multilayered media:** Dyadic Green's function for multilayered structures has been extensively used for calculating microwave thermal emission from layered media (Tsang *et al.*, 1974), thermal emission from 1-D photonic crystals (Narayanaswamy and Chen, 2005), power generation in near-field TPV systems (Park *et al.*, 2008), and near-field energy transfer between bodies with thin film coatings (Francoeur *et al.*, 2008; Fu and Tan, 2009). Figure 2 shows the schematic of a multilayered structure containing $N$ thin films sandwiched between two semi-infinite half spaces. Properties of the layers are different and are assumed to vary only in the $z$-direction. The layers can be metallic, dielectric or even be a vacuum gap and can have a temperature gradient across them. The dyadic Green's function between any two layers $s$ and $l$ in Fig. 2 is given by (Park *et al.*, 2008)

$$\overline{\overline{\mathbf{G}}}_e(\mathbf{x}, \mathbf{x}', \omega) = \frac{i}{4\pi} \int \frac{\beta d\beta}{\gamma_s} F(\beta) e^{i\beta(r-r')} \quad (7)$$

where

$$F(\beta) = A e^{i(\gamma_l z - \gamma_s z')} \hat{\mathbf{e}}_l^+ \hat{\mathbf{e}}_s^+ + B e^{i(-\gamma_l z - \gamma_s z')} \hat{\mathbf{e}}_l^- \hat{\mathbf{e}}_s^+ +$$
$$C e^{i(\gamma_l z + \gamma_s z')} \hat{\mathbf{e}}_l^+ \hat{\mathbf{e}}_s^- + D e^{i(-\gamma_l z + \gamma_s z')} \hat{\mathbf{e}}_l^- \hat{\mathbf{e}}_s^- \quad (8)$$

Here, the subscript $s$ denotes a source layer and $l$ is the receiving layer. Note that $\hat{\mathbf{e}}^+$ and $\hat{\mathbf{e}}^-$ are two unit vectors, which are given by $\hat{\mathbf{e}}_l^+ = \hat{\mathbf{e}}_l^- = \hat{\mathbf{r}} \times \hat{\mathbf{z}}$ for $s$-polarization and $\hat{\mathbf{e}}_l^\pm = (\beta\hat{\mathbf{z}} \mp \gamma_l\hat{\mathbf{r}})/k_l$ for $p$-polarization, respectively. The coefficients $A$,$B$,$C$, and $D$ can be determined using the transfer matrix formulation (Zhang, 2007; Park *et al.*, 2008; Francoeur *et al.*, 2009).

There are four terms in the expression of $F(\beta)$ because EM waves in each layer can be decomposed into upward and downward components due to multiple reflections at each interface. The first two terms account for the upward and downward waves in the $l$-th layer, respectively, which are induced by the upward waves in the source medium. Likewise, the last two terms denote the two waves in $l$-th layer due to the downward waves in the source medium (Tsang *et al.*, 2004). It should be pointed out that the terms having $\hat{\mathbf{e}}_s^-$ become zero if the source is in the bottom semi-infinite medium while the $l$-th layer is located above, and the terms having $\hat{\mathbf{e}}_l^-$ become zero if the $l$-th layer is the top semi-infinite medium or if there is free emission from multilayered structures. When both the source and receiver layers are semi-infinite, Eq. (7) will reduce to Eq. (6).

## 2.3. Dielectric Functions

Besides the fluctuation-dissipation theorem and dyadic Green's function, the dielectric function of materials should also be discussed to better understand near-field thermal radiation and its interactions with materials. If nonlinear optical effects are ignored, the polarization $\mathbf{P}$ is related to the electric field as $\mathbf{P}(\mathbf{x},\omega) = \varepsilon_0 \chi_e(\mathbf{x},\omega)\mathbf{E}(\mathbf{x},\omega)$, where $\chi_e(\mathbf{x},\omega)$ is the electric susceptibility of the medium and $\varepsilon_0$ is the permittivity of vacuum (Griffiths, 2012). The electric susceptibility indicates the degree of polarization of a dielectric material in response to the incident electric field, depending on the microscopic structure of the medium. The electric displacement vector $\mathbf{D}$ can be expressed as

$$\mathbf{D}(\mathbf{x},\omega) = \varepsilon(\omega)\mathbf{E}(\mathbf{x},\omega) \tag{9}$$

where $\varepsilon(\omega)$ is the dielectric function or relative permittivity of the medium and is related with the electric susceptibility as $\varepsilon(\omega) = \varepsilon_0[1+\chi_e(\omega)]$. It should be noted that the spatial dependence term in the susceptibility and the relative permittivity drops out under the local assumption. This local assumption remains valid for near-field thermal radiation unless the vacuum gap is extremely small (less than 1 nm distance). In the extreme proximity, the dielectric function becomes *nonlocal* and its wavevector dependence must be considered (Joulain, 2008). Recently, Chapuis *et al.* (2008a) calculated the near-field heat transfer between two semi-infinite gold plates using non-local dielectric function models and compared their results with the heat flux calculated using the Drude model for gold. They found that the non-local dielectric function saturates the near-field thermal radiation as the vacuum gap approaches zero, whilst local dielectric function erroneously diverges the thermal radiation .

Equation (9) represents the displacement of charges inside the material upon the incidence of electric waves. Thus the dielectric function is the key property in understanding the light-matter interactions, and needs to be further discussed. Under the local assumption, the following sections will discuss two models of the dielectric function, the Drude model for metals (and semiconductors) and the Lorentz model for dielectrics.

**Drude model for metals and semiconductors:** The Drude model describes the frequency-dependent conductivity of metals and can also be extended to free-carriers in semiconductors. In a metal, electrons in the outermost orbits are "free" to move in accordance with the external electric field. The dielectric function of a metal can be modeled by considering the electron movement under the electric field and is related to the conductivity by (Zhang, 2007)

$$\varepsilon(\omega) = \varepsilon' + i\varepsilon'' = (n + i\kappa)^2 = \varepsilon_\infty - \frac{\sigma_0/\tau}{\varepsilon_0(\omega^2 + i\omega/\tau)} \tag{10}$$

where $\varepsilon_\infty$ accounts for high-frequency contributions, $\tau$ is the relaxation time (inverse of scattering rate), $\sigma_0$ is the dc conductivity, and $n$ and $\kappa$ are the refractive index and extinction coefficient, respectively. Based on Eq. (10), the real and imaginary parts of the dielectric function can be

expressed as $\varepsilon' = n^2 - \kappa^2$ and $\varepsilon'' = 2n\kappa$, respectively. The plasma frequency is defined as $\omega_p = \sqrt{\sigma_0/(\tau\varepsilon_0)}$, which is in the ultraviolet region for most metals. When $\omega < \omega_p$, $n$ becomes smaller than $\kappa$ and $\varepsilon'$ becomes negative. At very low frequencies ($\omega\tau \ll 1$), the real part of the dielectric function is much smaller than the imaginary part, and therefore, $n \approx \kappa$. Generally speaking, metals become highly reflective in the visible and infrared regions.

**Lorentz model for dielectrics:** Unlike metals, the electrons in a dielectric are bound to molecules and cannot move freely. In contrast to free electrons, bound charges experience a restoring force given by the spring constant in addition to the damping force given by the scattering rate. There exist different kinds of oscillators in a real material, such as bound electrons or lattice ions. The response of a single-charge oscillator to a time-harmonic electric field can be extended to a collection of oscillators. Assuming $N$ types of oscillators in a dielectric, the corresponding dielectric function can be given as (Zhang, 2007)

$$\varepsilon(\omega) = \varepsilon_\infty + \sum_j^N \frac{\omega_{p,j}^2}{\omega_{0,j}^2 - \omega^2 - i\omega/\tau_j} \tag{11}$$

where $\omega_{p,j}$, $\omega_{0,j}$, and $\tau_j$ may be viewed as the plasma frequency, resonance frequency and the relaxation time of the $j$-th oscillator, respectively. Since the parameters for the Lorentz model are more difficult to be modeled as compared to those for the Drude model, they are considered as adjustable parameters that are determined from fitting. It can be observed from Eq. (11) that for frequencies far greater or lower than the resonance frequency, the extinction coefficient becomes negligible and the dielectrics are completely transparent. Absorption is appreciable only when an interval (i.e., $1/\tau_j$) is around the resonance frequency. Therefore, the dielectric becomes highly reflective near the resonance frequency, and the radiation inside the material is rapidly attenuated or dissipated. The spectral region with a large imaginary part of the dielectric function is also called the region of resonance absorption.

## 2.4. Surface Plasmon (or Phonon) Polaritons

Another radiative phenomenon that is worthwhile to discuss here is the optical plasmon (or phonon) polariton. Plasmons are quasiparticles associated with oscillations of plasma, which is a collection of charged particles such as electrons in a metal or semiconductor (Raether, 1988). Plasmons are longitudinal excitations of electron charges that can occur either in the bulk or at the interface. The field associated with a plasmon is confined near the surface, while the amplitude decays away from the interface. Such a wave propagates along the surface, and it is called a surface electromagnetic wave. Surface plasmons can be excited by electromagnetic waves and are important for the study of optical properties of metallic materials, especially near the plasma frequency, which usually lies in the ultraviolet.

In addition to the requirement of evanescent waves on both sides of the interface, the polariton dispersion relations given below must be satisfied (Raether, 1988; Park *et al.*, 2005):

$$\frac{k_{1z}}{\varepsilon_1} + \frac{k_{2z}}{\varepsilon_2} = 0 \quad \text{for TM waves} \tag{12}$$

$$\frac{k_{1z}}{\mu_1} + \frac{k_{2z}}{\mu_2} = 0 \quad \text{for TE waves} \tag{13}$$

This means that the sign of permittivity must be opposite for media 1 and 2 in order to couple a surface polariton with a TM wave. A negative $\text{Re}(\varepsilon)$ exists in the visible and near infrared for metals like Al, Ag, W, and Au. When Eq. (12) is satisfied, the excitation of surface plasmon polariton (SPP) interacts with the incoming radiation and causes strong absorption. Lattice vibration in some dielectric materials like SiC and $SiO_2$ can result in a negative $\text{Re}(\varepsilon)$ in the mid-infrared. The associated surface electromagnetic wave is called a surface phonon

polariton (SPhP). On the other hand, magnetic materials having negative permeability are necessary to excite a surface polariton for a TE wave. Some metamaterials can exhibit negative permeability in the optical frequencies, and negative index materials exhibit simultaneously negative permittivity and permeability in the same frequency region. Therefore, both TE and TM waves may excite SPPs with negative index materials (Park et al., 2005) or with bilayer materials of alternating negative $\varepsilon$ and $\mu$, the so-called single negative materials (Fu et al., 2005).

The condition for the excitation of surface polaritons is that the denominator of Fresnel's reflection coefficient be zero. A pole in the reflection coefficient is an indication of a resonance. Taking a TM wave for example, one can solve Eq. (12) to obtain (Zhang, 2007)

$$k_x = \frac{\omega}{c}\sqrt{\frac{\mu_1/\varepsilon_1 - \mu_2/\varepsilon_2}{1/\varepsilon_1^2 - 1/\varepsilon_2^2}} \tag{14}$$

This equation is called the polariton dispersion relation, which relates the frequency with the parallel component of the wavevector. For nonmagnetic materials, it becomes

$$k_x = \frac{\omega}{c}\sqrt{\frac{\varepsilon_1\varepsilon_2}{\varepsilon_1 + \varepsilon_2}} \tag{15}$$

One should bear in mind that the permittivities are in general functions of the frequency. For a metal with a negative real permittivity, the normal component of the wavevector is purely imaginary for any real $k_x$, because $(\mu\varepsilon\omega^2)/c^2 < 0$. Thus, evanescent waves exist in metals regardless of the angle of incidence.

The requirement of evanescent waves on both sides of the interface prohibits the coupling of propagating waves to the surface polaritons. Figure 3 qualitatively shows a dispersion curve of surface polaritons from Eq. (15) along with the dispersion line of the light propagating in a

dielectric having a refractive index nd, suggesting that the propagating light cannot excite the surface polariton. In order to couple propagating light with surface polaritons, we critically need a coupler that can shift the dispersion line of the light to match the parallel (or in-plane) wavevector component to that of the surface polaritons (Raether, 1988). Two conventional surface polariton couplers being widely accepted are a metal-coated prism and a metallic grating structure, whose configurations and mechanisms of light-SP(h)P coupling are schematically illustrated in Figs. 3 and 4. For a metal-coated prism coupler (or Kretschmann coupler), the in-plane wavevector of the incident light becomes $k_x = n_p k_0 \sin\theta$, where $n_p$ is the refractive index of the prism and $k_0 = \omega/c$ is the propagating wavevector in vacuum, when the light is incident on the metallic thin film of the prism side with the incidence angle $\theta$. Owing to the large refractive index of the prism, the dispersion line of the incident light shifts to a greater $k_x$, or to the right in Fig. 3(b), to intersect with the dispersion curve for the surface polariton: A metal-coated prism can excite the surface polariton.

When the light is incident on the grating structure as shown in Fig. 4(a), the Bloch-Floquet condition becomes $k_{x,j} = k_x + 2\pi j/\Lambda$, where $j$ is the diffraction order and $\Lambda$ is the grating period. The in-plane wavevector of the diffracted light can increase by a factor of $2\pi j/\Lambda$ depending on the diffraction order, shifting the light dispersion to couple with the SPP. It should be noted that the grating coupler can excite multiple surface polaritons even at the normal incidence. Figure 4(b) shows the reduced dispersion relation for a binary grating made of Ag with $\Lambda = 1.7~\mu m$ (Zhang, 2007). The dispersion curves (dash-dotted



(a) A metal grating coupler



(b) Dispersion relation



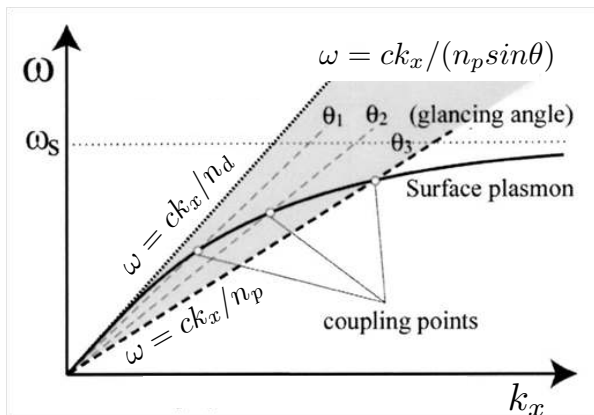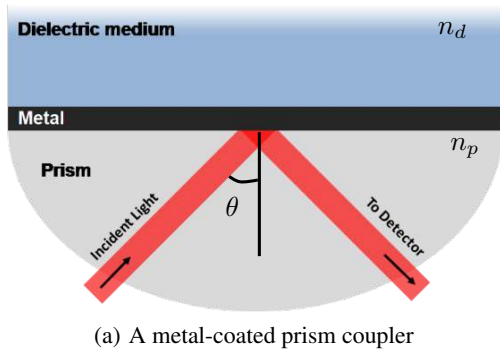(a) A metal-coated prism coupler



(b) Dispersion relation

**Fig. 3** (a) Schematic diagrams of a metal-coated prism surface polariton coupler and (b) dispersion curves.
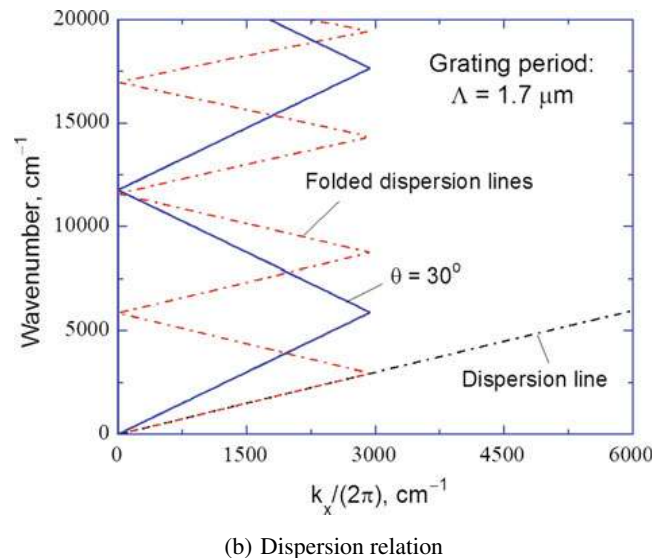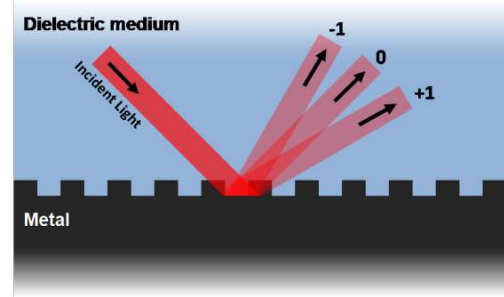
**Fig. 4** (a) Schematic diagrams of a metal grating surface polariton coupler and (b) Dispersion relation of SPP as manifested by an Ag grating (Zhang, 2007). Note that $k_x = (\omega/c)\sin\theta$.

lines) are folded. The solid lines correspond to an incidence angle of 30° and are also folded. The intersections identify the location where SPPs can be excited for a TM wave incidence, when the magnetic field is parallel to the grooves.

The excitation of surface polaritons makes a significant effect on near-field thermal radiation. As briefly mentioned in the introduction, the enhancement of heat transfer rate in near-field thermal radiation is because photon tunneling enables evanescent EM waves to carry radiative energy across the vacuum gap. Among the involved evanescent waves, those that match with the dispersion relation of the surface polariton will resonantly enhance the absorption of the evanescent EM fields. Thus near-field radiative heat transfer can be greatly enhanced with the surface polariton excitation. Moreover, surface polaritons play a crucial role in tailoring the spectral and directional radiative properties of materials. For example, coherent thermal emission can be realized by exciting surface polaritons in grating structures and truncated photonic crystals. Further discussion is deferred to later sections

## 3. NEAR-FIELD RADIATIVE ENERGY TRANSFER BETWEEN TWO SEMI-INFINITE MEDIA

### 3.1. Formulation of Near-Field Radiation

Consider the structure shown in Fig. 1, where both the emitter and receiver are $n$-doped silicon. The emitter and receiver are assumed to be at 400 and 300 K, respectively. The dielectric function model of doped Si may be modeled as a combination of Drude term and other contributions (Fu and Zhang, 2006) and the details are described in (Basu et al., 2010a,b). The total heat transfer between two media can be expressed as (Basu et al., 2009)

$$q''_{\text{net}} = \frac{1}{\pi^2} \int_0^\infty \left[ \Theta(\omega, T_1) - \Theta(\omega, T_2) \right] X(\omega) d\omega \quad (16)$$

where $X(\omega) = \int_0^\infty s(\omega, \beta) d\beta$. Note that the integration of $s(\omega, \beta)$ over $\omega$ gives a weighted function to modify the Planck blackbody distribution function. Expression of $s(\omega, \beta)$ is different for propagating ($\beta < \omega/c$) and evanescent ($\beta < \omega/c$) waves,

$$s_{\text{prop}}(\omega, \beta) = \frac{\beta(1 - \rho_{01}^s)(1 - \rho_{02}^s)}{4|1 - r_{01}^s r_{02}^s e^{i2\gamma_0 d}|^2} + \frac{\beta(1 - \rho_{01}^p)(1 - \rho_{02}^p)}{4|1 - r_{01}^p r_{02}^p e^{i2\gamma_0 d}|^2} \quad (17)$$

and,

$$s_{\text{evan}}(\omega, \beta) = \frac{\text{Im}(r_{01}^s)\text{Im}(r_{02}^s)\beta e^{-2\text{Im}(\gamma_0)d}}{|1 - r_{01}^s r_{02}^s e^{-2\text{Im}(\gamma_0)d}|^2} + \frac{\text{Im}(r_{01}^p)\text{Im}(r_{02}^p)\beta e^{-2\text{Im}(\gamma_0)d}}{|1 - r_{01}^p r_{02}^p e^{-2\text{Im}(\gamma_0)d}|^2} \quad (18)$$

In Eqs. (17) and (18), the first term on the right-hand side refers to the contribution of $s$-polarization or TE wave, while the second term refers to the contribution of $p$-polarization or TM wave. Note that $r_{0j}^s = (\gamma_0 - \gamma_j)/(\gamma_0 + \gamma_j)$ and $r_{0j}^p = (\varepsilon_j \gamma_0 - \gamma_j)/(\varepsilon_j \gamma_0 + \gamma_j)$ are the Fresnel reflection coefficients for $s$- and $p$-polarization, respectively, at the interface between vacuum and medium $j$ (1 or 2). On the other hand, $\rho_{0j} = |r_{0j}|^2$ is the far-field reflectivity at the interface between vacuum and medium $j$. When different doping levels are considered, the location of the peak in $s(\omega, \beta)$ shifts towards higher frequencies with increased doping level.

Notice that $s(\omega, \beta)$ is independent of temperature and contains all the information about the material properties as well as the geometry of the emitting media. The predicted radiative heat transfer between two doped Si plates is plotted in Fig. 5(a) as a function of the vacuum gap width (Basu et al., 2010b). Both plates are maintained at the same doping level, which is varied from $10^{18}$ to $10^{21}$ cm$^{-3}$. The dotted line with circles is the radiative heat flux between two blackbodies. The net heat flux at
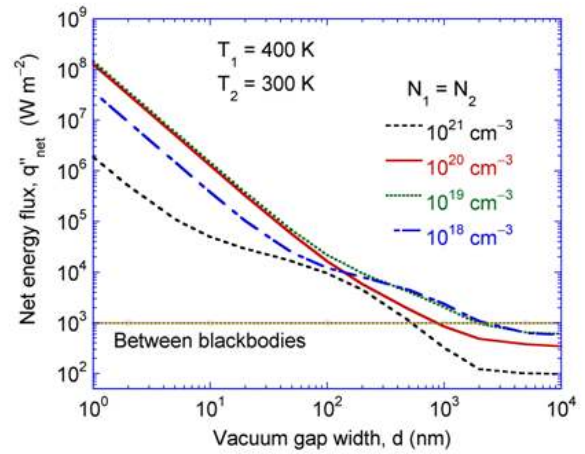


(a) Net energy flux vs. Vacuum gap width
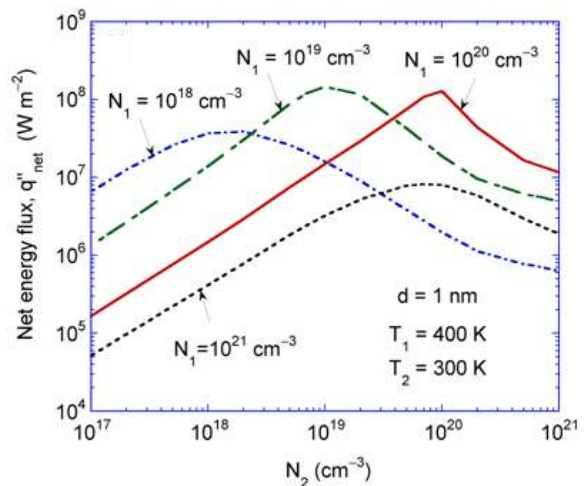


(b) Net energy flux vs. Doping concentration

**Fig. 5** Net energy flux between medium 1 (at 400 K) and medium 2 (at 300 K) versus the gap width for Si at different doping levels. The dash-dotted line refers to the net energy transfer between two blackbodies maintained at 400 and 300 K, respectively; and (b) effect of doping on the net energy transfer between two doped Si plates separated by 1 nm vacuum gap (Basu et al., 2010b).

$d = 1$ nm between $10^{19}$ or $10^{20}$ cm$^3$ doped Si plates can exceed that between two blackbodies by five orders of magnitude, because of photon tunneling and surface waves. Increase in the doping level of Si does not always enhance the energy transfer. In fact, the radiative heat transfer is the smallest for $10^{21}$ cm$^3$ doped Si plates as compared with other doping levels considered here. At $d > 200$ nm, doping concentrations between $10^{18}$ and $10^{19}$ cm$^3$ yield the largest radiative heat transfer, which is comparable to that between SiC and SiC. A detailed parametric study has been performed to determine the ideal Drude or Lorentz dielectric functions that yield the largest near-field enhancement (Wang et al., 2009). Figure 5(b) illustrates the effect of doping concentration on nanoscale energy flux when the vacuum gap width is fixed at $d = 1$ nm. The doping level of medium 1 is represented as $N_1$ while that for medium 2 is represented by $N_2$. Generally speaking, surface waves are better coupled when the two media have similar dielectric functions. As a result there exist peaks when $N_1 \approx N_2$, at doping levels up to $10^{20}$ cm$^3$.

The enhancement of near-field radiation in metallic and polar

materials can be well explained by surface polaritons. The coupling of SP(h)Ps allows a significant increase in the function given in Eq. (18) for evanescent waves. Furthermore, for magnetic materials, the enhancement can occur for both $s-$ and $p-$polarizations, resulting in multiple spectral peaks in near-field radiative transfer (Wang *et al.*, 2009; Joulain *et al.*, 2010; Zheng and Xuan, 2011). It should be noted that for intrinsic Si or dielectric materials without strong phonon absorption bands, the tunneling is limited and saturate at extremely small distances. Also, for good metals, the SPP excitation frequency is too high to significantly enhance thermal radiation unless the distance is less than 1 nm (Wang *et al.*, 2009; Basu and Francoeur, 2011b). Figure 6 illustrates the surface wave effects on the enhancement of near-field thermal radiation by comparing the contour plots of $s(\omega, \beta)/2\pi$ for SiC plates separated at 100 nm in Fig. 6(a) and for $10^{20}$ cm$^3$ $n-$doped Si plates separated at 10 nm in Fig. 6(b). Only TM waves are compared here since the contribution of TE waves is negligibly small. For simplicity, $\beta$ is normalized with respect to $\omega/c$. The brightest color represents the peak value at $\omega_m = 1.79 \times 10^{14}$ rad/s and $\beta_m = 50\omega/c$ for SiC, and at $\omega_m = 2.67 \times 10^{14}$

rad/s and $\beta_m = 62\omega/c$ for doped Si. The contribution of propagating waves ($\beta < \omega/c$) to the overall heat transfer is negligible. As mentioned earlier, the resonance energy transfer in the near field around $\omega_m$ is due to SPhP for SiC and SPP for doped Si, respectively.

The calculated dispersion curves for surface polaritons between two SiC and doped Si plates are also plotted as dashed lines in Figs. 6(a) and 6(b), respectively. Due to the coupling of surface polaritons at vacuum-SiC and vacuum-doped Si interfaces, there exist two branches of dispersion curves for the p polarization as follows:

$$\text{Symmetric mode}: \quad \frac{\gamma_0}{\varepsilon_0} + \coth\left(-\frac{i\gamma_0 d}{2}\right) \cdot \frac{\gamma_1}{\varepsilon_1} = 0 \quad (19a)$$

$$\text{Asymmetric mode}: \quad \frac{\gamma_0}{\varepsilon_0} + \tanh\left(-\frac{i\gamma_0 d}{2}\right) \cdot \frac{\gamma_1}{\varepsilon_1} = 0 \quad (19b)$$

The lower-frequency branch corresponds to the symmetric mode, and the higher-frequency branch represents the asymmetric mode (Park *et al.*, 2005). Note that for both doped Si and SiC, the dispersion relation becomes almost flat at $\omega_{max}$ implying that surface polaritons can be excited in a wide range of $\beta$, being responsible for the enhancement of thermal radiation through photon tunneling (Lee and Zhang, 2008).

### 3.2. Upper Limit of Near-Field Heat Flux

For nonmagnetic materials, when $\beta \gg \omega/c$ (evanescent waves), we have $\gamma_1 \approx \gamma_2 \approx \gamma_0 \approx i\beta$. As a result, for dielectrics, $r_{01}^s$ and $r_{01}^s$ are negligibly small, and the contribution of TE waves can be ignored. Furthermore, $r_{01}^P \approx (\varepsilon_1 - 1)/(\varepsilon_1 + 1)$ and $r_{02}^P \approx (\varepsilon_2 - 1)/(\varepsilon_2 + 1)$ are independent of $\beta$. Hence, Eq. (18) can be simplified as

$$s_{evan}(\omega, \beta) \approx \frac{\text{Im}(r_{01}^P)\text{Im}(r_{02}^P)\beta e^{-2\beta d}}{\left|1 - r_{01}^P r_{02}^P e^{-2\beta d}\right|^2} \quad (20)$$

However, for metals, the contribution from TE waves is more significant when $\omega/c = \beta = \sqrt{|\varepsilon_1|}\omega/c$, whereas the contribution from TM waves is more important for $\beta \gg \sqrt{|\varepsilon_1|}\omega/c \gg \omega/c$ (Chapuis *et al.*, 2008a). As a result, for metals, heat transfer due to TM waves becomes dominant at very short distances.

Using the relation, $\text{Im}\left[(\varepsilon - 1)/(\varepsilon + 1)\right] = (2\varepsilon'')/|\varepsilon + 1|^2$, and assuming identical permittivity for both media, the spectral heat flux from 1 to 2 in the limit $d \to \infty$ is given by (Basu and Zhang, 2009a)

$$q_{\omega,1-2}'' \approx \frac{4\Theta(\omega, T_1)}{\pi^2 d^2} \int_{\xi_0}^{\infty} \frac{\varepsilon''^2 e^{-2\xi}\xi d\xi}{|(\varepsilon + 1)^2 - (\varepsilon - 1)^2 e^{-2\xi}|^2} \quad (21)$$

where $\xi = \beta d$, $\xi_0 = d\omega/c$, and $\varepsilon''$ is the imaginary part of the dielectric function. As observed from Eq. (21) the heat flux will be inversely proportional to $d^2$ in the proximity limit. This means that the heat flux will diverge as $d \to 0$ and its physical significance has been debated among researchers. It should be noted that the $d^{-2}$ dependence is for contribution from the $p-$polarized electromagnetic waves only, since the contribution from the $s-$polarized waves will asymptotically reach a constant as $d \to 0$. As the vacuum gap decreases, the energy transfer shifts to large values of the parallel wavevector component. A cutoff in the order of the lattice constant is imposed as the minimum spatial wavelength, which subsequently sets a maximum wavevector component parallel to the interfaces (Volokitin and Persson, 2004). The imposed cutoff limits the number of modes for photon tunneling. Consequently, the radiative heat flux will experience a reduction as $d \to 0$.

In order to consider the upper limit of near-field radiative heat flux, $X(\omega)$ shown in Eq. (16) should be modified to $X(\omega) = \int_0^{\beta_c} s(\omega, \beta)d\beta$ to take into account the upper limit of the integration. Electrons in solids move in a periodic potential characterized by the Bloch wave, with a maximum wavevector of $\pi/a$ at the edge of the first Brillouin zone. Here, $a$ is the lattice constant, which is on the order of interatomic distance. This posts a limit on the smallest surface wavelength or cutoff wavevector
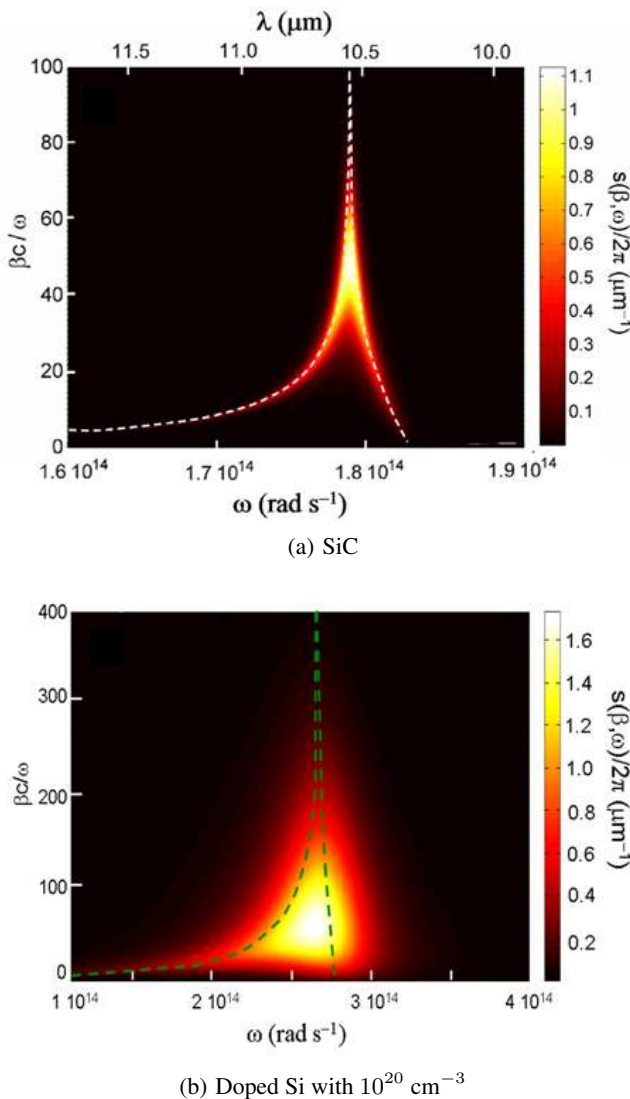


(a) SiC



(b) Doped Si with $10^{20}$ cm$^{-3}$

**Fig. 6** Contour plot of $s(\omega, \beta)/2\pi$ for (a) SiC and (b) $n$-doped Si for doping concentration of $10^{20}$ cm$^{-3}$. Note that the parallel wavevector component is normalized to the frequency. The dashed curves represent the two branches of the surface-polariton dispersion (Lee and Zhang, 2008; Basu *et al.*, 2010b).

parallel to the surface (Volokitin and Persson, 2004). Take a typical value of $a$ as 0.5 nm and note that there exists a maximum of $X$, i.e., $X_{\max} = \beta_c^2/8$. There exists an upper limit of the near-field radiative heat flux given by (Basu and Zhang, 2009a; Volokitin and Persson, 2004)

$$q_{\max}'' = X_{\max} \frac{k_{\mathrm{B}}^2}{6\hbar}(T_1^2 - T_2^2) = \frac{k_{\mathrm{B}}^2 \beta_{\mathrm{c}}^2}{48\hbar}(T_1^2 - T_2^2) \qquad (22)$$

for nonmagnetic materials. Note that $q_{\max}''$ is the ultimate maximum heat flux and is only achievable when $d \to 0$. It is found that metals with a large imaginary part in the infrared can help reach such a limit at extremely small distances (Pendry, 1999). For distances greater than a few nanometers, however, the situation is different. Basu and Zhang (2009a) considered a case in which both the emitter and receiver are assumed to have frequency-independent permittivity in order to identify the expression of the complex dielectric constant that will result in maximum heat flux. It should be noted that such a constant dielectric function cannot exist in reality because of the violation of Causality. When $X$ was plotted against $\varepsilon'$ and $\varepsilon''$ in a 3D plot or a 2D contour for given $d$ (say 10 nm), it was found that $X_{\max}$ corresponds to $\varepsilon' = -1$ at which surface waves exist.

Figure 7 shows the calculated radiative heat flux between the two media ($T_1 = 300$ K and $T_2 = 0$ K) as a function of the vacuum gap for different values of $\varepsilon'$ and $\varepsilon''$ (Basu and Zhang, 2009a). In most cases, $\varepsilon'$ is fixed at $-1$. For the sake of comparison, the energy transfer between two SiC plates is also shown in the figure using a frequency-dependent dielectric function. At 300 K, the upper limit of near-field heat flux is $1.4 \times 10^{11}$ W/m², which is represented as the dashed horizontal line. The radiation flux between two blackbodies is 459 W/m², which is several orders of magnitude smaller than near-field radiative transfer. The cutoff in $\beta$ sets an upper limit on the maximum energy transfer between the two media. Hence, for each of the dielectric functions, there exists an optimal vacuum gap width ($d_m$) that allows the maximum energy transfer. For $\varepsilon = -1 + i0.1$, it can be seen from Fig. 7 that $d_m = 0.6$ nm, which also
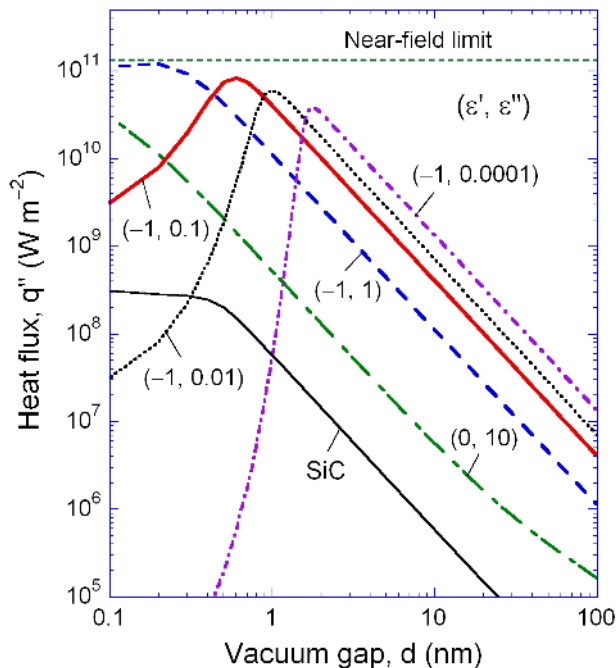


**Fig. 7** Plot of radiative heat flux versus gap width for different dielectric functions (Basu and Zhang, 2009a). The temperatures of the two media are set to be 300 K and 0 K. The dielectric function is assumed to be frequency independent, except that for SiC for which the Lorentz model at 300 K is used.

maximizes $X$. The value of $d_m$ decreases with increasing $\varepsilon''$, implying that the reduction in the energy transfer begins to take place at smaller vacuum gaps. Furthermore, the $d^{-2}$ dependence in the energy transfer exists only when $d > d_m$. At $d > 2$ nm, increasing $\varepsilon''$ results in a decrease of the heat flux. When $\varepsilon = 0 + i10$, the radiative heat flux is generally much smaller than those with $\varepsilon' = -1$ but will keep increasing towards the upper limit as $d$ unrealistically approaches zero. For the selected dielectric functions with $\varepsilon' = -1$ and $\varepsilon'' \ll 1$, the energy transfer can be orders of magnitude greater than that between SiC plates. This is due to the assumed frequency-independent dielectric function, which results in the excitation of surface waves at almost every frequency. While no such materials can exist, the results provide some hints of appropriate dielectric functions that will result in optimal heat flux at different vacuum gaps. By introducing the cutoff in $\beta$, even for SiC, the $d^{-2}$ trend ceases to exist at $d < 0.6$ nm. Instead, the near-field radiative transfer reaches a plateau below $d = 0.5$ nm. Wang et al. (2009) performed a design optimization of the parameters in the Drude model and Lorentz model that can result in the highest near-field radiative flux at given distance and temperatures.

### 3.3. Penetration Depth in Nanoscale Thermal Radiation

Traditionally, radiation penetration depth in a solid, also called skin depth or photon mean free path, is defined as $\delta_\lambda = \lambda/(4\pi\kappa)$, where $\kappa$ is the extinction coefficient as discussed earlier. A film whose thickness is six times the skin depth can be treated as opaque in most applications. In the optical spectrum, the penetration depth of noble metals is usually $10-20$ nm. For an evanescent wave, such as that induced under the total internal reflectance setup when light is incident from an optically denser medium to a rarer medium, the skin depth may be defined according to the $1/e$ attenuation of the field as $\delta = 1/\mathrm{Im}(\gamma)$, where $\gamma$ (purely imaginary) is the wavevector component perpendicular to the interface in the optically rarer medium. The electric and magnetic fields will decay exponentially and become negligible at a distance greater than about one wavelength. Hence, the skin depth is expected to be several tenths of a wavelength in a dielectric medium. However, in near-field radiation especially when SP(h)Ps are excited, an extremely small skin depth (on the order of the vacuum gap $d$) may exist even though the dominant wavelengths are in the infrared (Basu and Zhang, 2009b). Furthermore, the skin depth is proportional to the separation distance. In essence, the skin depth in near-field thermal radiation is a function of the vacuum gap as well as material properties (Basu and Francoeur, 2011b).

For a very small gap, while $\omega_m$ (see Fig. 6) remains constant as $d$ decreases, the energy transfer is shifted towards a larger $\beta$, leading to greater near-field enhancement. For $\beta \gg \sqrt{\varepsilon_j}\omega/c$, $\gamma_j \approx i\beta$ or $\mathrm{Im}(\gamma_j) \approx \beta$. There exists an evanescent wave (in medium 3) whose amplitude decays according to $e^{-\beta(z-d)}$. Hence, the skin depth of the field becomes $\delta_{\mathrm{F}} \approx 1/\beta$ and the power penetration depth becomes $\delta_{\mathrm{P}} \approx 1/(2\beta)$. Using the multilayer Green's function, the $z-$component of the Poynting vector, which is proportional to the heat flux, can be calculated both inside the emitter and the receiver. The spectral and total Poynting vector distributions are plotted in Fig. 8 for SiC. The ordinate is normalized to the Poynting vector inside the vacuum gap. The energy flux in the emitter increases towards the surface, remains constant in the vacuum gap, and decreases in the receiver away from the surface. When the abscissa is $z/d$, the results are nearly the same for 1 nm $< d <$ 100 nm. Surprisingly, the distributions are symmetric in the emitter and the receiver. The $1/e$ decay line is shown as the horizontal dashed line so that the penetration depth can be evaluated. Note that the calculated Poynting vector is integrated over all $\beta$ values. As mentioned earlier, when SPP is excited, the energy transfer is pushed towards large $\beta$ values; hence, the spectral penetration depth has a minimum near $\omega_{\mathrm{m}}$.

As shown in Fig. 8, the penetration depth is approximately $0.19d$ at 10.54 $\mu$m, where SPP is excited at the vacuum-SiC interfaces. The actual minimum penetration depth is located at 10.47 $\mu$m, corresponding to the
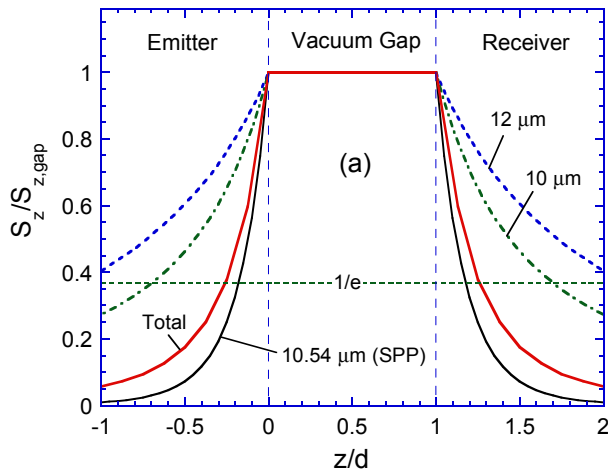
**Fig. 8** The distributions of the spectral and total Poynting vector ($z$-component) near the surfaces of the emitter and receiver (refer to Fig. 1), both made of SiC, normalized to that in the vacuum (Basu and Zhang, 2009b).

maximum of $X(\omega)$. The penetration depth increases towards longer or shorter wavelengths, and the overall penetration depth based on the total energy flux is $0.25d$, which is about 30% greater than $\delta_P$ evaluated at $\omega_m$ and $\beta_m$. For a thin vacuum gap, the SPhP dispersion is shifted to large $\beta$ values, resulting in a shorter penetration depth. Hence, a 10-nm coating of SiC can act as an optically thick medium when $d = 10$ nm as predicted in Refs. (Francoeur *et al.*, 2008; Fu and Tan, 2009). When $d < 1$ nm, the penetration depth is less than a monolayer, implying that the SiC emitter is completely a 2D solid. It should be mentioned that $\delta_P$ cannot be arbitrarily small. When $d$ is comparable to or less than the interatomic distance, the radiative transfer cannot be explained by the local electromagnetic theory. Obviously, in such case, one cannot use its bulk dielectric function and also cannot set $\beta_c$ as infinity. Note that with magnetic materials, surface waves can be excited by both TE and TM waves. The penetration depth in near-field radiation between metamaterials has also been examined (Basu and Francoeur, 2011b).

### 3.4. Energy Streamlines

The direction in near-field transfer cannot be determined by the wavevector as in the case of a propagating wave. From the wave point of view, phonon tunneling is through the coupling of evanescent waves since there exist a forward decaying and backward decaying waves in the vacuum gap, both with purely imaginary $\gamma$, the $z$−component of a wavevector. In such case, the Poynting vector represents the direction of energy flow and the trace of Poynting vectors provides the energy streamlines (ESLs), which can be used to elucidate the energy propagation like fluid flow (Zhang and Lee, 2006). Due to the random fluctuation of charges, the Poynting vectors are decoupled for different values of $\beta$ (Lee and Zhang, 2008; Lee *et al.*, 2007). The ESLs are laterally displaced as they leave the surface of the emitter and reach the surface of the receiver. This lateral displacement is called a *lateral shift* (Basu and Zhang, 2009a), which is different from the well-known Goos-Hänchen shift (Zhang and Lee, 2006), may be important to determining the lateral dimension of the real system which can be modeled as infinite plates in near-field radiation.

Figure 9 shows the ESL projected to the $x$−$z$ plane at $\lambda = 10.55$ $\mu$m and $d = 100$ nm for $\beta = 40\omega/c$ in all three media for $p$−polarized waves (Lee *et al.*, 2007). The magnitude of magnetic field is overlaid as depicted by the colored contours (i.e., the brighter color indicates the greater value). To calculate the magnetic field, thin-film optics is employed with an assumption that a plane wave is incident from medium 1. The emission originated deeper from the surface than the radiation penetration depth could not reach the SiC-vacuum interface. Hence, the field distribution is
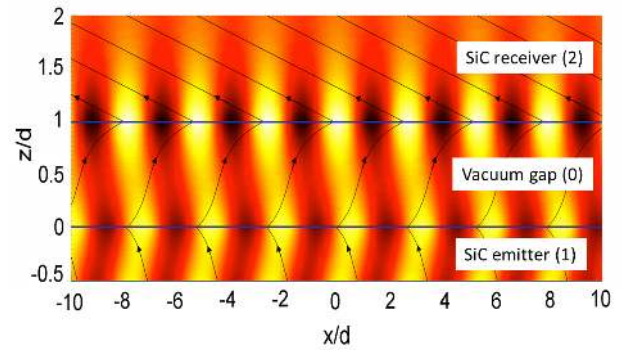


**Fig. 9** Energy streamlines for TM waves in SiC-vacuum-SiC for $d = 100$ nm. The magnitude of the magnetic field is denoted by colored contours and plotted along with the ESLs (Lee *et al.*, 2007).

plotted in the vicinity of the vacuum gap. It can be seen from Fig. 9 that negative refraction of energy path occurs at the interfaces between SiC and vacuum due to the opposite sign of their dielectric functions. The energy streamlines are curved except for medium 3 where no backward waves exist. The magnetic field oscillates in the lateral direction as a result of the excitation of SPhPs.

Basu *et al.* (2011) applied fluctuational electrodynamics in multi-layered structures to directly trace the energy streamlines not only in the gap and receiver but also in the emitter. It was found that when surface waves are excited, there is a larger lateral shift inside the emitter. Figure 10 shows the ESLs for combined TE and TM waves at $d = 10$ nm with different $\beta$ values. Note that for propagating waves, $\beta^* = \beta c/\omega < 1$ and the shape of ESLs is independent of $d$ in the proximity limit. For evanescent waves, the contribution of TM waves to the near-field radiation is dominant. At the SPhP frequency, ESLs for the same $\beta d$ value are essentially the same. The resonance conditions may be denoted by $\omega_m$ and $\beta_m$. When $d$ is very small, $\omega_m$ depends little on $d$, whereas $\beta_m$ is inversely proportional to $d$ as mentioned previously. The value corresponds to $\beta_m^* = \beta_m c/\omega_m = 450$ when $d = 10$ nm. For propagating waves, all ESLs are located inside the conical surfaces bounded by the ESL at $\beta = \omega/c$ (Basu and Zhang, 2009a). The ESLs inside the emitter and the vacuum gap are curved much more for evanescent waves than for propagating waves, as it is assumed to be semi-infinite and no backward waves exist. Because the receiver is treated as non-emitting (i.e., at zero absolute temperature), the streamlines in the receiver are straight lines. Figure 10(b) suggests that the largest lateral shift occurs inside the emitter and the lateral shift increases with $\beta$. Hence, it is important to take the lateral shift inside the emitter into consideration when determining the minimum area needed for the emitter and receiver to be approximated as infinitely extended plates. In the receiver, the lateral shift can be written as $\theta(z, \omega, \beta) = \tan^{-1}(\varepsilon''/\varepsilon')$ when $\beta^* \gg 1$ (or $\beta \gg \omega/c$). Hence inside the receiver, ESLs for evanescent waves are parallel as seen in Fig. 10(b). But this is not so for propagating waves when ESLs can intercept each other. The results obtained from this study will facilitate the design of experiments for measuring nanoscale thermal radiation. The method discussed above can be extended to the study of energy flux and streamlines between layered structures and materials with coatings.

### 4. NEAR-FIELD RADIATIVE ENERGY TRANSFER IN VARIOUS MEDIA

The previous section has made intensive discussions on the near-field radiative heat transfer between two half-spaces separated with a vacuum gap, including when they have thin coatings. We now discuss radiative heat transfer between different geometries, in particular between two spheres in Sec. 4.1, between a sphere and a half-space in Sec. 4.2, and between other geometries such as cylinders and gratings in Sec. 4.3, when they are held at different temperatures and separated in vacuum. In
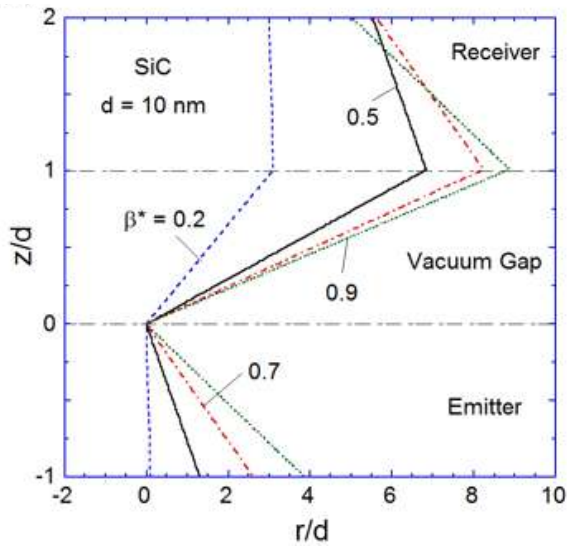
(a) Propagating waves
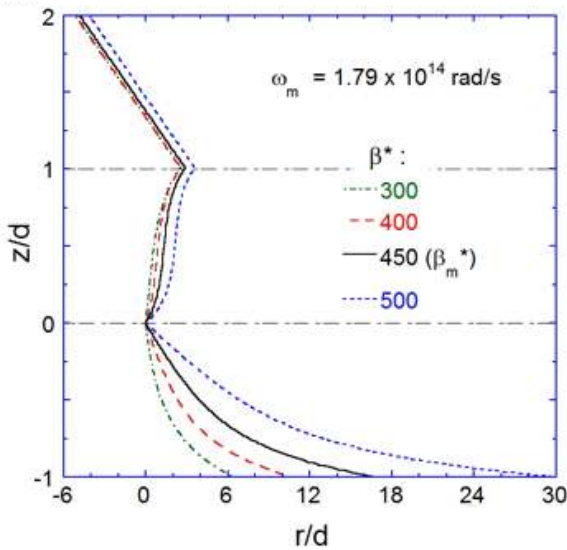


(b) Evanescent waves

**Fig. 10** ESLs for combined TE and TM waves at the SPhP frequency for SiC with $d = 10$ nm at different $\beta^* = \beta c/\omega$ values: (a) propagating waves; (b) evanescent waves (Basu *et al.*, 2011).

addition, near-field radiative energy transport in emerging materials will also be discussed in Sec. 4.4.

**4.1. Near-Field Radiative Heat Transfer between Two Spheres**

Near-field radiative heat transfer between two spherical nanoparticles has been theoretically predicted by modeling the nanoparticles as fluctuating dipoles (Volokitin and Persson, 2001; Dorofeyev, 2008; Chapuis *et al.*, 2008b). When there are two spherical nanoparticles whose dielectric constants are $\varepsilon_1$ and $\varepsilon_2$, the spectral power dissipated in particle 2 by the electromagnetic field induced by particle 1 can be written using the dipolar approximation as

$$Q_{1 \to 2}(\omega) = \varepsilon_0 \frac{\omega}{2} \text{Im}(\alpha_2) |\mathbf{E}_{\text{inc}}(\mathbf{x}_2, \omega)|^2 \qquad (23)$$

where $\mathbf{x}_2$ is the position of the particle 2 and $\alpha_2 = 4\pi R^3(\varepsilon_2-1)/(\varepsilon_2+2)$ is the polarizability of a sphere of radius $R$ having the relative permittivity of $\varepsilon_2$. The electric field incident on the particle 2, $\mathbf{E}_{\text{inc}}(\mathbf{x}, \omega)$, is

created by the thermal fluctuating dipole of particle 1 at temperature $T_1$: $\mathbf{E}_{\text{inc}}(\mathbf{x}_2, \omega) = \mu_0 \omega^2 \overline{\overline{\mathbf{G}}}_e(\mathbf{x}_2, \mathbf{x}_1, \omega) \cdot \mathbf{p}$. Here, $\overline{\overline{\mathbf{G}}}_e(\mathbf{x}_2, \mathbf{x}_1, \omega)$ is the electric dyadic Green's function between two dipoles in vacuum and expressed as (Domingues *et al.*, 2005)

$$\overline{\overline{\mathbf{G}}}_e(\mathbf{x}_2, \mathbf{x}_1, \omega) = \frac{ke^{ikd}}{4\pi} \left[ \left( \frac{1}{kd} + \frac{i}{(kd)^2} + \frac{1}{(kd)^3} \right) \overline{\overline{\mathbf{I}}} + \right.$$
$$\left. (\hat{\mathbf{u}}_r \hat{\mathbf{u}}_r) \left( \frac{3}{(kd)^3} - \frac{3i}{(kd)^2} - \frac{1}{kd} \right) \right] \qquad (24)$$

where $d = |\mathbf{x}_2 - \mathbf{x}_1|$ is the distance between the sphere centers, $\overline{\overline{\mathbf{I}}}$ is the identity tensor, and $\hat{\mathbf{u}}_r \hat{\mathbf{u}}_r$ is the dyadic notation of unit vectors. Because of thermal fluctuations, particle 1 has a random electric dipole that yields the correlation function of the dipole:

$$\langle p_m(\omega) p_n^*(\omega') \rangle = \frac{4\varepsilon_0}{\pi\omega} \text{Im}[\alpha_1(\omega)] \Theta(\omega, T_1) \delta_{mn} \delta(\omega - \omega') \qquad (25)$$

Equation (25) is in fact the primitive form of Eq. (1). By combining the above equations, we finally obtain the thermal conductance between two dipoles due to near-field radiative heat transfer that can be expressed as (Domingues *et al.*, 2005):

$$G_{12}(T) = \frac{3}{4\pi^3 d^6} \int_0^\infty \frac{d\Theta(\omega, T)}{dT} \text{Im}[\alpha_1(\omega)] \text{Im}[\alpha_2(\omega)] d\omega \qquad (26)$$

It should be noted that radiative heat transfer between two spheres has the $d^{-6}$ spatial dependence, which is typical of the dipole-dipole interactions. The thermally fluctuating dipole at one nanoparticle induces electromagnetic field on the other nanoparticle to cause the second dipole to fluctuate. Equation (26) suggests that near-field radiative thermal conductance between two nanoparticles has a resonant behavior when the polarizability $\alpha$ has a resonance, or the dielectric constant approaches $-2$ in $\alpha_{1(2)} = 4\pi R_{1(2)}^3(\varepsilon_{1(2)}-1)/(\varepsilon_{1(2)}+2)$. Provided that the surface polariton resonance occurs when the dielectric constant approaches $-1$ in case the material is interfaced with the vacuum (Raether, 1988), this resonant behavior is not directly related with the surface polariton resonance: instead, is named as the localized surface polariton resonance − grouped oscillations of the charge density confined to nanostructures (Hutter and Fendler, 2004). The localized surface polariton resonance appears in the visible range for metals and in the infrared for polar materials.

While the dipole approximation elucidates the $d^{-6}$ dependence of the near-field radiative heat transfer between two spheres, this dependence is valid only when $R \ll \lambda_T$ and $d \gg R_1 + R_2$, where $\lambda_T$ is the characteristic wavelength defined from Wien's displacement law (Zhang and Wang, 2012), and $R_1$ and $R_2$ are radii of nanoparticles. However, near contact, the near-field radiative thermal conductance deviates drastically from the dipole approximation. This deviation results from the fact that when particles become very close, the charge distributions become nonsymmetric and cannot be described merely as two interacting dipoles (Pérez-Madrid *et al.*, 2008). For cases when the dipole approximation is not valid, calculation of near-field thermal radiation between two spheres becomes computationally challenging, mainly due to the difficulty in determining the dyadic Green's function. More realistic Green's function for the two-sphere configuration has been suggested by approximating nanoparticles as fluctuating multipoles (Pérez-Madrid *et al.*, 2008) and by implementing the vector spherical wave expansion method (Narayanaswamy and Chen, 2008). Narayanaswamy and Chen (2008) investigated the scattering between two spheres by expanding the electromagnetic field in terms of the vector spherical waves at each sphere and re-expanding the vector spherical waves of one sphere with the vector spherical waves of the second sphere to satisfy the boundary conditions. Recurrence relations for vector spherical waves were used to reduce the computational demands in determining translation coefficients of each spherical wave function

term. Due to complexities in the formulations, the equations of the dyadic Green's function for two spheres are not included here but can be found from Narayanaswamy and Chen (2008) for a detailed derivation and Sasihithlu and Narayanaswamy (2011) for the convergence limit of the vector spherical wave expansion approach.

Domingues *et al.* (2005) attempted to overcome the limitation of the dipole-approximation by using the molecular dynamics (MD) scheme. After computing all the atomic positions and velocities as function of time using Newton's second law, $\sum_j \mathbf{f}_{ij} = m_i \ddot{\mathbf{x}}_i$, where $m_i$ and $\ddot{\mathbf{x}}_i$ are the atomic mass and acceleration and $\mathbf{f}_{ij}$ is the interatomic force exerted by atom $j$ on atom $i$, the power exchange between two nanoparticles (NP$_1$ and NP$_2$) is computed as the net work done by a particle on the ions of the other particle:

$$Q_{1 \leftrightarrow 2} = \sum_{\substack{i \in \mathrm{NP}_1 \\ j \in \mathrm{NP}_2}} \mathbf{f}_{ij} \cdot \mathbf{v}_j - \sum_{\substack{i \in \mathrm{NP}_1 \\ j \in \mathrm{NP}_2}} \mathbf{f}_{ji} \cdot \mathbf{v}_i \qquad (27)$$

The interatomic force $\mathbf{f}_{ij}$ is derived from the van Beest, Karmer, and van Santen (BKS) interaction potential (van Beest *et al.*, 1990), in which a Coulomb and a Buckingham potentials are included.

When the interparitlce distance is larger than the radii of spheres, i.e., $d \geq 4R$ for identical spheres with the radius $R$, the aforementioned methods (Domingues *et al.*, 2005; Pérez-Madrid *et al.*, 2008; Narayanaswamy and Chen, 2008) have a good agreement with the dipole approximation (e.g., Volokitin and Persson, 2001): See Fig. 11. However, at smaller interparticle distances, they show different trends. Figure 11(a) shows that the thermal conductance predicted in Refs. (Domingues *et al.*, 2005) and (Pérez-Madrid *et al.*, 2008) has a higher gap dependence than $d^{-6}$, resulting in four orders of magnitude higher than the dipole approximation in the intermediate distance range, i.e., $2R < d < 4R$. This enhanced heat transfer appears to be due to the contribution of multipolar Coulomb interactions (Pérez-Madrid *et al.*, 2008). However, as shown in Fig. 11(b), the thermal conductance calculated by Narayanaswamy and Chen (2008) asymptotically approaches a $d^{-1}$ slope when the interparticle gap distance is much smaller than the particle radius. This slope change is consistent with the result of the proximity approximation or the Derjaguin approximation (Derjaguin *et al.*, 1956). In the Derjaguin approximation, the radiative heat flux between curved surfaces is approximated as the summation of heat fluxes between flat plates that integrate to form the profile of curved surfaces. The consequent thermal conductance is simplified as $G_{12} \approx \pi R \cdot d \cdot h_r(d, T)$, where $h_r$ is the radiative heat transfer coefficient between flat surfaces. From the previous studies (Mulet *et al.*, 2002; Fu and Zhang, 2006; Basu and Zhang, 2009a), it was found that $h_r$ has $d^{-2}$ dependence in the near-field regime. Therefore, the proximity approximation predicts the $d^{-1}$ dependence in the near-field thermal conductance, which is in contradiction to the $> d^{-6}$ dependence predicted in (Domingues *et al.*, 2005; Pérez-Madrid *et al.*, 2008). While this discrepancy is likely due to the difference in the considered nanoparticle sizes, i.e., $R = 0.72$ nm $- 1.79$ nm (Domingues *et al.*, 2005; Pérez-Madrid *et al.*, 2008) versus $R \geq 20$ nm (Narayanaswamy and Chen, 2008), further theoretical and experimental investigations are required to resolve this contradiction in near-field thermal radiation between two spheres.

Another unresolved issue regarding the near-field thermal radiation between spheres is the drastic decrease of thermal conductance when they become in contact. MD simulation (Domingues *et al.*, 2005) predicts that the contact thermal conductance would be 2-3 orders of magnitude lower than the conductance just before contact: see Fig. 11(a). This drastic reduction is still an open question that cannot be explained with the fluctuation-dissipation theorem. At such sub-nanometric distance, nanoparticles cannot be treated as a thermodynamic system at local equilibrium: fluctuation-dissipation theorem is not valid (Pérez-Madrid *et al.*, 2003). The knowledge gap on the thermal conductance change
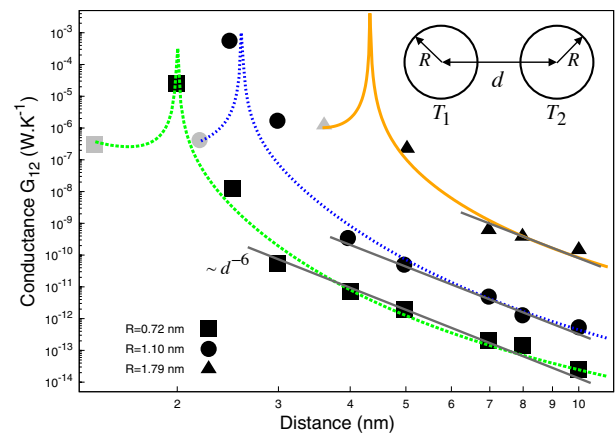


(a) Pérez-Madrid *et al.* (2009)
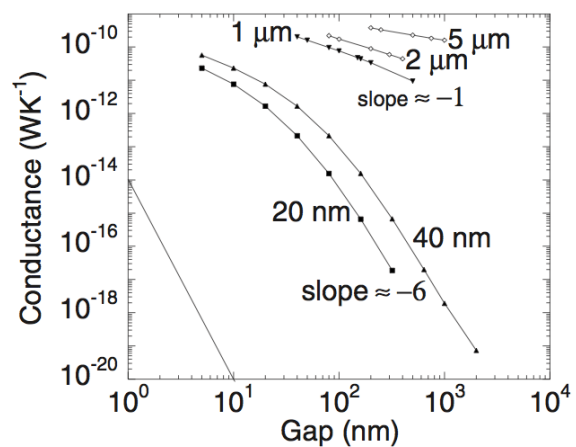


(b) Narayanaswamy and Chen (2008)

**Fig. 11** Thermal conductance between two identical micro/nanospheres computed (a) in the framework of mesoscopic nonequilibirum thermodynamics (Pérez-Madrid *et al.*, 2009) and (b) using the vector spherical wave expansion method (Narayanaswamy and Chen, 2008). The inset illustrates the sphere-sphere configuration for the identical sphere case. In (a), the marks represent molecular dynamics data obtained by Domingues *et al.* (2005), where particles with effective radius $R = 0.72$, 1.10 and 1.79 nm were considered. The grey points represent the conductance when the particles are in contact. When bigger spheres are considered in (b), the gap dependence asymptotically approaches $d^{-1}$ as the gap distance further decreases below the dipole approximation limit. (Figures reprinted with permission of the American Physical Society.)

upon contact was explored by implementing the mesoscopic nonequilibrum thermodynamics for the calculation of the random current density, based on the assumption of the validity of the second law in the phase space (Pérez-Madrid *et al.*, 2009). The computed near-field radiative thermal conductance has a strong enhancement as $d$ decreases below around double the radii of spheres, $d < 4R$, due to multipolar Coulomb interactions (Pérez-Madrid *et al.*, 2008). However, it sharply falls to the contact thermal conductance when both nanoparticles are in contact. This sharp reduction is attributed to an intricate conglomerate of energy barriers inherent to the amorphous character of nanoparticles, which is generated by the strong interaction (Pérez-Madrid *et al.*, 2009).

### 4.2. Near-Field Radiative Heat Transfer between a Sphere and a Half Space

In this part, we discuss near-field thermal radiation between a small spherical particle and a semi-infinite medium, which can be considered as a simplified model of the scanning tunneling microscopy or scanning thermal microscopy (Volokitin and Persson, 2001). Similarly to the previous section, the small particle can be approximated as a dipole of radius $R$ with dielectric constant $\varepsilon_P(\omega)$ and temperature $T_P$. The semi-infinite surface is maintained at temperature $T_B$ and has the dielectric constant $\varepsilon_B(\omega)$. The center of the particle is at a distance $d$ above the interface. Then, the spectral mean power radiated by the half space and absorbed by the particle can be written as (Mulet et al., 2001)

$$P_{B\to P}(\omega) = \frac{2\omega^4}{\pi c^4} \mathrm{Im}[\varepsilon_B(\omega)] \mathrm{Im}[\alpha_P(\omega)] \Theta(\omega, T_B)$$
$$\sum_{n,m=x,y,z} \int_B \left| G_{nm}(\mathbf{x}_P, \mathbf{x}', \omega) \right|^2 d^3\mathbf{x}' \quad (28)$$

When the fluctuating currents inside the particles radiate into the half space and dissipate, the locally dissipated power per unit volume at a point $\mathbf{x}$ inside the space can be written as

$$P_{P\to B}(\mathbf{x}, \omega) = \frac{2\omega^4}{\pi c^4} \mathrm{Im}[\varepsilon_B(\omega)] \mathrm{Im}[\alpha_P(\omega)] \Theta(\omega, T_B)$$
$$\sum_{n,m=x,y,z} |G_{nm}(\mathbf{x}, \mathbf{x}_P, \omega)|^2 \quad (29)$$

where $\alpha_P(\omega) = 4\pi R^3[\varepsilon_P(\omega) - 1]/[\varepsilon_P(\omega) + 2]$ is the polarizability of the dipole and $\mathbf{G}_{nm}(\mathbf{x}, \mathbf{x}', \omega)$ is $(n, m)$ component of the dyadic Green's function at $\mathbf{x}$ due to a point source at $\mathbf{x}'$ in a system constituted by two semi-infinite media whose dielectric constants are either 1 if $z \geq 0$ or $\varepsilon_B(\omega)$ if $z < 0$. It should be noted that the dipole polarizability needs to be corrected to take into account the interaction between the dipole and the interface when $d$ is comparable to $R$ (Dorofeyev, 1998).

When $P_{B\to P}(\omega)$ is calculated for a SiC spherical particle at temperature $T_P = 300$ K of radius $R = 5$ nm at different distances above the SiC surface (Mulet et al., 2001), two peaks are observed at frequency $\omega_1 \approx 1.756 \times 10^{14}$ rad/s and $\omega_2 \approx 1.787 \times 10^{14}$ rad/s, each of which corresponds to the localized surface polariton resonance of the SiC particle (i.e., $\mathrm{Re}[\varepsilon_P] = -2$) and the surface polariton resonance on the SiC surface (i.e., $\mathrm{Re}[\varepsilon_B] = -1$), respectively. Moreover, near-field radiative heat transfer increases showing the $d^{-3}$ dependence as $d$ decreases, enhanced by several orders of magnitude than the far-field thermal radiation. Another example is shown in Fig. 12, which plots $P_{P\to B}(\omega)$ emitted from a SiC particle of radius $R = 25$ nm heated at $T_P = 1000$ K to a gold surface right below the particle. There is a sharp peak at $\sim$930 cm$^{-1}$, corresponding to $\omega \approx 1.756 \times 10^{14}$ rad/s or 10.6 $\mu$m when the tip is near the surface, suggesting that the heated SiC particle emits a quasi-monochromatic thermal radiation at around 10.6 $\mu$m in the near-field regime.

It should be noted again that the dipole approximation for a sphere is valid when $R \ll \lambda_T$ and $d \geq 2R$. In the other extreme case, i.e., $d \ll R \sim \lambda_T$, the dipole approximation may not be valid, and instead we should use the proximity approximation (or Derjaguin approximation). Applying the proximity approximation for the sphere-flat surface case, the near-field thermal conductance has the $d^{-1}$ dependence, instead of $d^{-3}$. This result was experimentally validated as will be discussed in the following section. A further research was conducted to seek the shape dependence of near-field radiative heat transfer when a spheroidal metallic nanoparticle is in proximity to a planar metallic sample (Huth et al., 2010). By changing the aspect ratio of a spheroidal particle from 1/5 (long axis perpendicular to the surface) to 5 (long axis parallel to the surface) while fixing its volume, they predicted that the total radiative heat transfer between a gold spheroid at 100 K and a gold planar surface
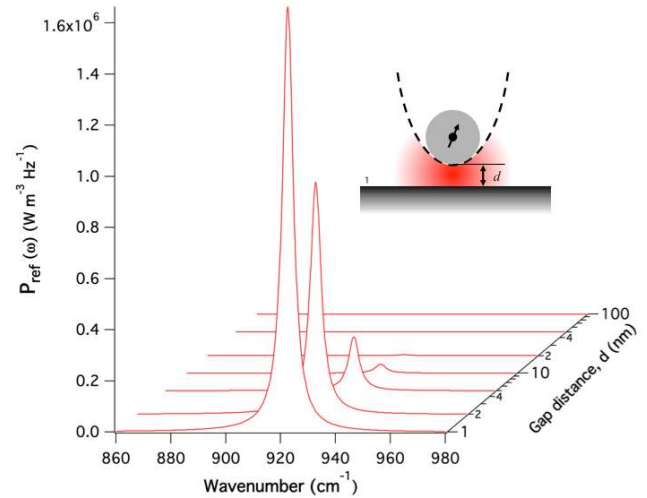


**Fig. 12** Mean spectral power radiated from the SiC particle (of radius $R = 25$ nm and held at $T_P = 1000$ K.) to the gold surface right below the particle.

at 300 K at the gap width of 100 nm changes from about half to two times of that between sphere and planar surface.

### 4.3. Near-Field Radiative Heat Transfer in Cylindrical Objects

While various geometries of nanostructures are being developed as potential candidates for efficient heat transfer sources, it is not an easy task to theoretically investigate radiative heat transfer from or between such nanostructures. The thermal radiation of long cylindrical objects whose thickness is in the range of the thermal wavelength is a good example, as it can be very different from the classical blackbody radiation described by Planck's law (Öhman, 1961). Recent experimental studies on thermal radiation of an antenna-like platinum microheater (Ingvarsson et al., 2007; Au et al., 2008), a single SiC whisker antenna (Schuller et al., 2009), thin tungsten wires (Bimonte et al., 2009) and individual carbon nanotubes (Fan et al., 2009; Singer et al., 2011) demonstrated that thermal radiation from sub-wavelength cylindrical emitters has coherent features and thus can be polarized depending on the orientation of the emitters. Polarization effects were also observed from the thermal radiation of carbon nanotube bundles (Li et al., 2003), which could be used to probe the degree of alignment inside the bundle. Some works (Schuller et al., 2009; Singer et al., 2011) further studied the polarized thermal radiation by developing a simple theoretical model based on the Mie theory and comparing with the measurement, revealing that the degree of polarization is affected by the optical conductance along with the geometry of the cylindrical thermal emitter. However, the Mie theory could not correctly deliver the frequency-dependence of the degree of polarization, requiring a more comprehensive theoretical model. The Kadar group at MIT has developed a general formalism to compute the heat radiation of arbitrary objects in terms of their classical scattering properties based on the fluctuation-dissipation theorem (Krüger et al., 2011; Golyk et al., 2012). They predicted that the degree of polarization of the emitted radiation depends on the cylinder radius: if the radius is much smaller than the thermal wavelength, the radiation is polarized parallel to the cylindrical axis and becomes perpendicular when the radius is comparable to the thermal wavelength.

Recently, near-field radiative heat transfer between cylinder-cylinder and cylinder-plate has been formulated. Carillo and Bayazitoglu (Carrillo and Bayazitoglu, 2011, 2012) modified the aforementioned vector spherical wave expansion approach (Narayanaswamy and Chen, 2008) for near-field sphere-to-sphere radiative exchange to make it applicable

to cylindrical geometry of nanorods. The computation results on silica nanorods clearly show strong near-field effect on radiative heat transfer for the cylinder-cylinder case, but uniquely from the spherical case, this near-field enhancement is due to the larger geometric surface area that enables more photon tunneling of evanescent waves. They also asymptotically computed a nanorod-to-plate geometric configuration, where a nanorod lies in parallel to the plane, by increasing the radius of a nanorod while the other nanorod radius is held constant until the corresponding radiative heat transfer rate converges. A cylinder-to-plate configuration where the cylinder axis is perpendicular to the plate was investigated and compared with a sphere-to-plate and a sharp tip-to-plate cases (McCauley, 2012). The near-field cylinder-to-plate heat transfer rate has a $\sim d^{-2}$ gap dependence while the sphere-to-plate case shows a $d^{-1}$ dependence, consistently with the proximity approximation. The tip-to-plate configuration has the least gap dependence in the near-field heat transfer rate and, interestingly, exhibits a local minimum heat flux directly below the tip that becomes deeper as the tip becomes sharper. The authors believe that this dip in the local heat flux is attributed to the more dipole-like radiative behaviors as the tip becomes sharper. While further experimental verifications need to be followed, the accumulated results manifest that a general numerical method to calculate near-field radiative heat transfer between arbitrary objects, including all the aforementioned geometries, is at hand.

### 4.4. Near-Field Radiative Heat Transfer in Emerging Materials

Most near-field thermal radiation studies to date have focused on naturally occurring materials, such as dielectrics, semiconductors, metals and polar materials. However, the advent of nanotechnology has enabled the integration of emerging materials, such as graphenes, photonic crystals, and metamaterials, in the near-field radiative heat transfer research. This section is thus devoted to provide up-to-date review of near-field radiation research where novel materials are involved.

**Graphene:** Graphene has recently received a keen attention due to its unique electronic (Novoselov et al., 2004, 2005), mechanical (Frank et al., 2007), and thermal (Lee et al., 2011) properties, thus has been actively explored for next-generation technologies (Geim and Novoselov, 2007). Among many graphene-based electronic and sensor applications, graphene field-effect transistors (FETs) are considered as a promising candidate that would resolve current challenges of Si-based FETs (Schwierz, 2010). However, heat generation and dissipation in the graphene FET must be fundamentally understood prior to its reliable operation in commercial integrated circuits.

Freitag et al. (2009) measured the temperature distribution of a biased single-layer graphene FET and found that 77% of the heat dissipation occurs at the gate stack (300 nm SiO$_2$ film on silicon) directly below the active graphene channel, having an effective graphene-SiO$_2$ interface heat transfer coefficient of $h_{\text{Gr}-\text{SiO}_2} \approx 2.4 \times 10^7$ W/m$^2$-K. Theoretical studies have followed to fundamentally understand the graphene-SiO$_2$ interfacial thermal interactions. Persson and Ueba (2010a,b) studied heat transfer mechanisms between graphene and amorphous SiO$_2$ in contact by including the heat transfer from the area of real contact as well as between the surfaces in the non-contact region, which may occur due to rough surfaces. Although it was concluded that most of the heat flows through the area of real contact, they were the first that considered near-field thermal radiation in graphene-involved configurations. However, their near-field radiation calculation was based on the assumption that the free carriers in graphene had vanishing drift velocity, which may cause significant discrpancies from actual behaviors of graphene. The effect of drift velocity on the graphene-SiO$_2$ near-field thermal radiation was explored by considering quantum fluctuations of free carriers along with thermal fluctuations in graphene (Volokitin and Persson, 2011). For nonsuspended graphene on SiO$_2$ (having a subnanometer separation), near-field radiation gives a significant contribution to the heat transfer in addition to the contribution of phononic coupling: the near-field radiative

heat transfer coefficient can reach $\sim 10^8$ W/m$^2$-K at $d = 0.35$ nm when the biased electric field is in the low and intermediate range. On the other hand, suspended graphene with separation in the order of 1 nm has the near-field radiative heat transfer coefficient of $\sim 10^4$ W/m$^2$-K, which is significantly less than for the nonsuspended graphene case but still $\sim 3$ orders of magnitude larger than the blackbody radiation limit ($h_{bb} \approx 5$ W/m$^2$-K).

Recently, two papers were concurrently published that analyzed the contributions of plasmons to near-field radiative heat transfer in graphene (Svetovoy et al., 2012; Ilic et al., 2012a). Both studies were motivated by the tunability of plasmon frequencies in graphene from terahertz to the near infrared by changing the electron density (Ju et al., 2011). Near-field radiative heat transfer between graphene-coated dielectrics can be larger than the best known materials for the radiative heat transfer — around two times the near-field radiative heat transfer coefficient between SiO$_2$ ($h_{\text{SiO}_2-\text{SiO}_2} \approx 300$ W/m$^2$-K at room temperature when the gap distance is $\sim 100$ nm), and can be reduced 100 times or so (Svetovoy et al., 2012). In addition, near-field radiative heat transfer between two graphene sheets can be enhanced up to three orders of magnitude the blackbody radiation limit as the gap distance is reduced to 10 nm (Ilic et al., 2012a). These unique radiative features of graphene may offer a potential for a novel, hybrid thermophotovoltaic/thermoelectric solid-state energy conversion platform, as reported in Ref. (Ilic et al., 2012b) that proposed the application of graphene as a thermal emitter in a near-field thermophotovoltaic system.

**Periodic Structures:** Near-field radiative heat transfer in periodic structures, such as *nanoporous media* (Biehs et al., 2011a), *gratings* (Biehs et al., 2011b), and *photonic crystals* (Ben-Abdallah et al., 2010; Rodriguez et al., 2011), has become a very interesting topic with promising future applications. By combining the fluctuation-dissipation theorem and the Maxwell-Garnett effective medium description for effective media, Biehs and his colleagues (2011a) studied radiative heat transfer between two semi-infinite nanoporous media, made of SiC having cylindrical inclusions oriented in the perpendicular direction to the surface. The obtained results reveal that for the small distance regime ($d < 100$ nm), the heat flux between the nanoporous media can be significantly larger than that between two homogeneous SiC plates in the same thermal conditions (e.g., $\sim 50\%$ larger radiative heat flux when nanoporous media have a 0.5 filling factor and are separated by $d = 10$ nm). This increase is seemingly due to additional surface waves arising at the uniaxial material-vacuum interface. The same numerical scheme was applied to near-field heat transfer between two misaligned 1-D gratings (Biehs et al., 2011b). As the twisting angle changes from the parallel grating configuration ($\phi = 0°$), the near-field radiative heat flux between gratings is modulated significantly, up to 90% reduction for the perpendicular ($\phi = 90°$) configuration when gold gratings with a filling factor of 0.3 are taken into account. This allows the manipulation of the heat flux at nanoscale.

Photonic crystals are another example of periodic structures. By periodically repeating dielectric or metallo-dielectric layers of high and low dielectric constants, the propagation of electromagnetic waves can be controlled to have a photonic band gap, i.e., wavelength band of disallowed photon propagation, giving rise to distinct optical phenomena such as inhibition of spontaneous emission, high-reflecting mirrors, and low-loss-waveguide (Yablonovitch, 1987; John, 1987). Due to such unique radiative properties, photonic crystals have been applied to manipulate thermal radiation, such as wavelength-selective thermal emission (Pralle et al., 2002; Lin et al., 2003; Narayanaswamy and Chen, 2005, 2004; O'Sullivan et al., 2005) and spectrally and directionally coherent thermal emission (Lee et al., 2005; Lee and Zhang, 2006a,b; Lee et al., 2008a). Near-field thermal radiation between photonic crystals has also been addressed with different approaches, including the use of dyadic Green's function along with the scattering matrix method (Francoeur et al., 2009), the expansion of Green tensors in terms of the intracavity fields (Ben-Abdallah et al., 2010), and the

finite-difference time-domain method (Rodriguez *et al.*, 2011). These theoretical investigations report that the strong coupling of surface Bloch states supported by photonic crystals makes near-field heat transfer several folds larger than that between two homogeneous plates at the same separation distance (Ben-Abdallah *et al.*, 2010). Moreover, even frequency-selective near-field radiative heat transfer is possible with careful design of photonic crystals (Rodriguez *et al.*, 2011).

**Metamaterials:** Metamaterials are broadly defined as any artificial material engineered to achieve material properties that may not be found in nature, but narrowly referred to as materials with negative refractive index (Pendry, 2000; Shelby *et al.*, 2001; Smith *et al.*, 2002). Metamaterials has emerged as a new frontier of optical and thermal radiation research, as it may realize innovative technologies such as superlenses, invisibility cloaks, and manipulation of radiative properties (Fu and Zhang, 2009; Liu and Zhang, 2011). Near-field radiative heat transfer between metamaterials is thus an attractive research topic that may pave the way to the development of novel thermal management or energy harvesting. Earlier studies demonstrated that surface polaritons could be excited for both *p*- and *s*-polarizations when the refractive index becomes negative (Ruppin, 2000, 2001; Park *et al.*, 2005). Later, radiative and nonradiative heat exchanges between metamaterials were conducted by considering fluctuations of electric and magnetic currents density in semi-infinite metamaterials (Joulain *et al.*, 2010). They showed that the excitation of magnetic polariton resonance (when the magnetic permeability becomes $-1$) and the ferromagnetic behavior of materials under a strong magnetization (when the magnetic permeability becomes large) yield novel channels for energy transfer enhancement. The enhancement factor of near-field radiation, normalized to the blackbody radiation, becomes in the order of $10^4$ in the extreme near-field regime (i.e., $5.31 \times 10^{-4} \lambda_p$, where $\lambda_p$ is the plasma wavelength), where heat transfer is dominated by polariton-like waves. Similar enhancement mechanisms of radiative heat transfer in near field were also found in different types of metamaterials, such as chiral metamaterials (Cui *et al.*, 2012) and SiC sphere-embedded potassium bromide (Francoeur *et al.*, 2011a), confirming that the presence of negative magnetic permeability in metamaterials is beneficial in enhancing near-field thermal radiation. More recently, hyperbolic metamaterials were also studied for potentially enhanced near-field radiation (Biehs *et al.*, 2012).

## 5. EXPERIMENTAL OBSERVATIONS OF NEAR-FIELD RADIATIVE HEAT TRANSFER

Due to difficulties in maintaining the nanoscale gap distance between the emitter and the receiver, experimental investigations of near-field thermal radiation have been rather limited. Cravalho *et al.* (1966), Domoto *et al.* (1969), and Hargreaves (1969) were among the first to measure the radiative flux of two parallel plates at cryogenic temperatures. Domoto *et al.* (1969) measured the radiative heat transfer at cryogenic temperatures between two copper plates at gaps from 1 to 10 $\mu$m. While the near-field heat transfer was 2.3 times greater than that of the far field, the measured heat flux was only 3% of the energy transfer between blackbodies. Hargreaves (1969) measured the near-field heat transfer between two chromium plates separated by vacuum gaps from 6 to 1.5 $\mu$m. At 1.5 $\mu$m vacuum gap, the near-field heat transfer at room temperature was five times greater than that in the far field. However, the measured heat flux was still only 40% of that between two blackbodies. In 1994, Xu *et al.* (1994) tried to measure near-field radiative heat transfer through a sub-micrometer vacuum gap by using an indium needle of 100 $\mu$m in diameter and a thin-film thermocouple on a glass substrate, but could not observe a substantial increase of radiative heat transfer. On the other hand, Muller-Hirsch *et al.* (1999) found that near-field radiation plays an important role in heat transfer between a STM thermocouple probe and a substrate. However, due to the limit of their experimental setup, they were not able to determine the absolute

value of near-field thermal radiation. This limit was overcome in their following work (Kittel *et al.*, 2005) by successfully calibrating the STM thermocouple probe, demonstrating the $d^{-3}$ dependence in the near-field thermal radiation from the surface to the thermocouple tip of $R = 60$ nm when the gap is larger than 10 nm. However, for gaps less than 10 nm, the measured heat flux saturates and differs from the divergent behavior of the predicted results. The authors attributed this difference to the spatial dependence of the dielectric function of materials.

Continuous efforts have been made to experimentally demonstrate the near-field enhancement of energy transfer for other relatively simple geometries, such as parallel plates separated by micro-particle spacers (Hu *et al.*, 2008) and microsphere-plate geometry (Narayanaswamy *et al.*, 2008; Shen *et al.*, 2009; Rousseau *et al.*, 2009; Shen *et al.*, 2012). The thermal conductance of near-field radiation was successfully measured for a gap distance as small as 30 nm by using a vertically aligned bimetallic AFM cantilever having a silica or gold-coated silica microsphere at the free end. The plate was heated to produce a temperature difference $\Delta T$ between the sphere and the plate, typically on the order of $10-20$ K, leading to the near-field radiative heat flux of the order of nanowatts. In order to measure such small heat flux, the measurement was conducted in a vacuum condition ($\sim 10^{-6}$ mbar). Near-field thermal radiation was measured by monitoring the deflection of the bimetallic cantilever, which has a minimum measurable temperature of $10^{-4}-10^{-5}$ K and a minimum detectable power of $5 \times 10^{-10}$ W (Narayanaswamy *et al.*, 2008). Comparison of their measurement with the Derjaguin approximation confirms that the near-field thermal radiation between the microsphere and flat surface is more than two orders of magnitude larger than that of blackbody radiation and has $d^{-1}$ dependence. At a $30 \pm 5$ nm gap, the heat transfer coefficient was measured to be $\sim 400$ W/m$^2$-K for Au-Au, which is around 4 times smaller than that for SiO$_2$-SiO$_2$ and much greater than the blackbody radiation limit of $\sim 5$ W/m$^2$-K (Shen *et al.*, 2012). Although the enhancement of near-field radiative heat transfer between SiO$_2$ surfaces can be explained with strong coupling of surface phonon polaritons (Shen *et al.*, 2009), the radiative heat transfer enhancement for the Au-Au case is somewhat counterintuitive since metals are highly reflective for infrared lights. However, the theoretical study of near-field radiation between metals reveals that although metals are highly reflective, thermal radiation emitted from the hot surface experiences multiple reflections in a nanoscale gap until eventually absorbed by the cold surfaces (Chapuis *et al.*, 2008b).

## 6. APPLICATIONS OF NEAR-FIELD RADIATIVE TRANSFER

### 6.1. Manipulation of Radiative Properties

Controlling the radiative properties has important applications in photonic and energy conversion systems such as solar cells and solar absorbers, thermophotovoltaic (TPV) devices, radiation filters, selective emitters, photodetectors, semiconductor processing, and optoelectronics (Zhang and Wang, 2011; Basu *et al.*, 2007; Zhang *et al.*, 2003; Zhu *et al.*, 2009). The performance of various devices can be greatly enhanced by the modification of the reflection, transmission, absorption and emission spectra using one-, two-, or three-dimensional micro/nanostructures. Surface microstructures can also strongly affect the directional behavior of absorption and emission due to multiple reflections and diffraction, allowing the radiative properties to be tailored. Because of the important applications to energy transport and conversion, the study of engineered surfaces with desired thermal radiative characteristics has become an active research area.
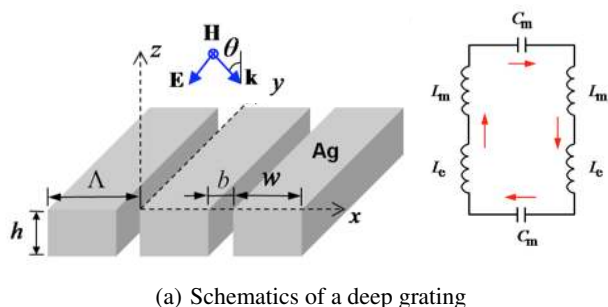
As briefly introduced in the previous section, photonic crystals have been studied to control the thermal emission to be wavelength-selective (Pralle *et al.*, 2002; Lin *et al.*, 2003; Narayanaswamy and Chen, 2005, 2004; O'Sullivan *et al.*, 2005) or to be spectrally and directionally coherent (Lee *et al.*, 2005; Lee and Zhang, 2006a,b; Lee *et al.*, 2008a).

For the application as wavelength-selective diffuse TPV emitters and infrared detectors, Chen and Zhang (2007, 2008) proposed the concept of complex gratings whose surface profile is superposed by two or more 1D grating profiles. The complex grating may improve simple 1D gratings by reducing the sharpness in the spectral peak and the directional sensitivity. Moreover, heavily-doped silicon complex gratings exhibit a broad band absorptance peak that is insensitive to the angle of incidence by properly choosing the carrier concentration and geometry. The peak wavelength can be engineered by changing either the height of the ridges or the period. Such a type of absorptance peak comes from the SPP excitation and is dominated by the first evanescent diffraction order.
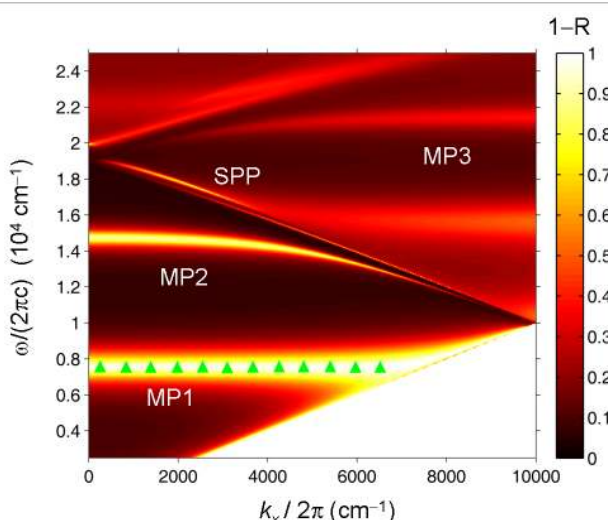
Recent studies on periodic gratings have revealed that localized magnetic polaritons (MPs), which are responsible for extraordinary transmission in metamaterials (Liu *et al.*, 2006, 2009), can also occur in periodic gratings to significantly alter the thermal radiative properties of the structure (Lee *et al.*, 2008c). Figure 13 illustrates the effect of MP for a deep grating structure (Wang and Zhang, 2009). The induced current flow, shown as red arrows, in the 1-D grating can be modeled by an equivalent LC circuit model shown in Fig. 13(a) and the included inset. The contour plot of $1 - R$, or the sum of the transmittance $T$ and absorptance $\alpha$, as a function of $\omega$ and $k_x$ is shown in Fig. 13(b). The radiative properties of considered structure are calculated with the rigorous coupled-wave analysis (RCWA) (Lee *et al.*, 2008b) and the

predicted resonance frequency from the LC model for the fundamental mode (MP1) is illustrated as triangles. Excellent agreement between the LC model and the RCWA results further confirms the mechanism of magnetic resonance. The bright bands indicate usually a strong transmission, but can also be associated with a strong absorption, due to the resonance behavior of SPPs or MPs. The inclined line close to the light line, which is then folded due to the Bloch-Floquet condition in the gratings, is associated with the excitation of SPP at the Ag-vacuum interface. Several relatively flat dispersion curves correspond to the fundamental, second, and third modes of MPs and are marked as MP1, MP2 and MP3 in the figure. The flatness of MP dispersion curves indicates their unique feature as directional independence. The directional independence of MPs can be understood by the diamagnetic response, as the oscillating magnetic field is always along the $y$-direction no matter what incident angles is for TM waves. It should be noted that, the cavity-like resonance or coupled SPPs were previously proposed to explain the resonance phenomenon in simple gratings, but MPs seem to more quantitatively account for the geometric effects on the resonance conditions (Wang and Zhang, 2009).

Another potential application of the MPs is the construction of coherent thermal emission sources. It has been demonstrated that a nanostructure consisting of a periodic metallic strips separated by a thin dielectric layer over an opaque metal film exhibits coherent emission characteristics (Lee *et al.*, 2008c; Zhang *et al.*, 2011). The coupling of the metallic strips and the film induces a magnetic response that is characterized by a negative permeability and positive permittivity. On the other hand, the metallic film intrinsically exhibits a negative permittivity and positive permeability in the near infrared. This artificial structure is equivalent to a pair of single-negative materials. By exciting surface MPs, large emissivity peaks can be achieved at the resonance frequencies, which are almost independent of the emission angle. This spectrally selective, diffuse thermal emission could be beneficially used for thermophotovoltaics if MPs are excited in the infrared range (Wang and Zhang, 2012). To this end, phonon-assisted MPs were also explored by designing deep SiC grating structures, observing similar features as metallic MP couplers (Wang and Zhang, 2011).

## 6.2. Near-Field Thermophotovoltaic Energy Conversion

It has been recently reported that the current global energy demand is approximately 14 TW and is expected to double to 25-30 TW by 2050 (Baxter *et al.*, 2009). When considering the serious energy dependence (i.e., more than 80% of the current energy consumption) on fossil fuels including oil, coal, and natural gas, raising prices of these energy sources and carbon-dioxide-driven global warming will pose a grave threat to the global economy and environment. Thus it is imperative to develop carbon-free, high-efficiency and low-cost renewable energy harvesting and recycling technologies.

Thermophotovoltaic (TPV) energy conversion is an energy harvesting technology that directly generates electric power from thermal sources emitting IR radiation. A TPV system consists of a thermal emitter and a TPV cell that is a $p$-$n$ junction semiconductor converting radiative energy to electric power (Basu *et al.*, 2007). Since wasted heat from many industrial processes (e.g., glass manufacturing or power plants) can be used as an IR emission source, TPV systems are considered as one of the promising techniques for the wasted energy recovery and recycling. Moreover, having no moving parts allows quiet and reliable operations in harsh environments, making TPV ideal in military or space applications (Nelson, 2003). When compared with other solid-state technologies, the energy conversion efficiency of TPV ($\sim$25%, Lin *et al.*, 2003) is higher than those of thermoelectric ($<\sim$15%, Chen, 2006) and thermionic ($<\sim$13%, Lee *et al.*, 2009) devices. However, the TPV efficiency is still low and, more seriously, its low power throughput is a big challenge in applying the TPV for effective energy recycling. Thermal radiation at low working temperatures is not a compelling energy source due to the $T^4$



(a) Schematics of a deep grating



(b) MP and SPP dispersion contour

**Fig. 13** Effect of magnetic polaritons (MPs) on the radiative properties of a single grating (slit array): (a) Schematic of a deep grating with th inset that depicts the equivalent LC circuit model; (b) Contour plots of the sum of absorptance and transmittance (i.e., $1 - R$) for a Ag grating with period $\Lambda = 500$ nm, $h = 400$ nm, and $b = 50$ nm. Triangle marks indicate the frequency of the fundamental mode predicted by the LC circuit model (Wang and Zhang, 2009).

dependence of the radiative power: for example, the blackbody emissive power at 600 K is only $\sim$7 kW/m$^2$, which is too small for thermal energy harvesting.

One solution for improving the power throughput and conversion efficiency of the TPV system may be to utilize near-field thermal radiation. The feasibility of the near-field TPV system has been investigated by several research groups. Pan et al. (2000) were the first to analyze the performance of near-field TPV systems. However, they used the same dielectric material for both the emitter and TPV cell to calculate the near-field energy enhancement, which is not only overly simplified but also impractical. Whale and Cravalho (2002) considered a more realistic system by using a fictitious Drude material with a low conductivity and InGaAs for the emitter and the TPV cell, respectively. Narayanaswamy and Chen (2003) theoretically demonstrated the effect of surface polaritons in improving the performance of near-field TPV systems. However, their work focused only on the thermal radiation enhancement, leaving questions on the near-field effect on the photocurrent generation. Laroche et al. (2006) provided an analysis on the performance and efficiency of near-field TPV systems based on the assumption of 100 % quantum efficiency in calculating the photocurrent generation; this may result in an overestimation of the TPV system performance. Park et al. (2008) performed a more realistic analysis of the power generation in a near-field TPV system by calculating the photocurrent generation in different regions of the TPV cell. Francoeur et al. (2011b) developed a coupled near-field thermal radiation and the charge and heat transfer model within the cell and stressed the thermal management issues in near-field TPV systems.

A near-field TPV energy conversion system consists of a TPV cell and the thermal source that are separated with a very small vacuum gap. Figure 14 illustrates a conceptual near-field TPV device used in (Park et al., 2008), where a tungsten thermal emitter is placed in proximity to a TPV cell within a subwavelength gap distance. In order to demonstrate the operation concept of TPV device, the thermal source is set to be made of tungsten and maintained at $T_H = 2000$ K, so that the characteristic wavelength of thermal emission is around 1.5 $\mu$m. As for the TPV cell, In$_{0.18}$Ga$_{0.82}$Sb is chosen because its energy bandgap of 0.56 eV is sufficiently low for the thermophotovoltaic energy conversion. Doping concentration of the $p$-layer is set to $10^{19}$ cm$^{-3}$ whilst the tellurium-doped $n$-layer has a doping concentration of $10^{17}$ cm$^{-3}$ (González-Cuevas et al., 2006). The concentration gradient of the majority carriers across the $p$-$n$ junction diffuses electrons from the $n$- to $p$-region, and
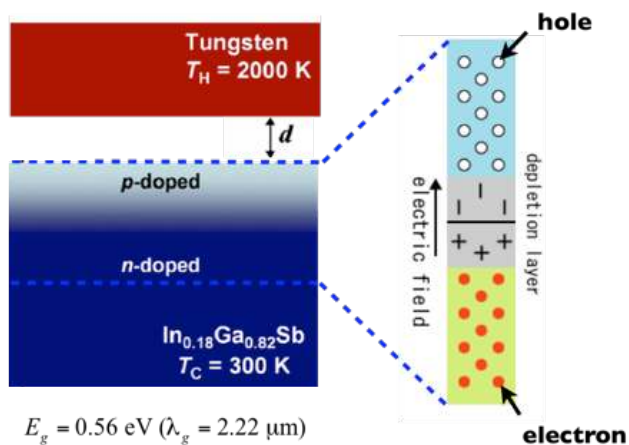


**Fig. 14** Schematic of a near-field TPV system, where In$_{0.18}$Ga$_{0.82}$Sb is used as the TPV cell material and plain tungsten is used as the emitter. Both the emitter and the cell material are modeled as semi-infinite media.

vice versa for the holes. As a result, the depletion region having only ionized dopants is formed, and its width is estimated to be 0.1 $\mu$m from the given doping concentrations (González-Cuevas et al., 2006). When thermal radiation is incident on the TPV cell, photons whose energy is greater than the bandgap energy $E_g$ will generate electron-hole pairs inside the TPV cell. However, some electron-hole pairs generated outside the depletion region will be recombined as they diffuse toward the edge of the depletion region. In order to predict the near-field thermophotovoltaic power generation, Park et al. (2008) first calculated the distribution of radiative energy absorption in the TPV cell due to near-field thermal radiation using the fluctuation dissipation theorem and dyadic Green's function for a multilayered structure, and calculated photocurrent generation in each region to have $J_\lambda(\lambda) = J_e(\lambda) + J_h(\lambda) + J_{dp}(\lambda)$, where $J_{e(h)}(\lambda)$ is the photocurrent generated in the $p(n)$-doped region and $J_{dp}(\lambda)$ is a drift current generated in the depletion region.

The performance of a TPV system can be evaluated through two efficiencies: the quantum efficiency $\eta_q$ and the conversion efficiency $\eta$. The quantum efficiency is the ratio of the number of electron-hole pairs used for the photocurrent generation to the number of photons absorbed. On the other hand, the conversion efficiency (or thermal efficiency) is the ratio of the electric power generated from a TPV cell to the absorbed radiative power. Figure 15(a) shows the total photocurrents integrated over all wavelengths as a function of the vacuum gap distance. In general, $J_h$ is greater than $J_e$ due to the large thickness of the $n$-region. However, when the vacuum gap is very small, i.e., $d < 4$ nm, $J_e$ becomes greater than $J_e$ because a significant amount of the near-field thermal radiation is absorbed very close to the surface. The sum of the three photocurrents is used to calculate the electrical power generated by the TPV cell. Apparently, the near-field enhancement occurs in both the thermal radiation and the electric power generation: see Fig. 15(b). From the calculated near-field thermal radiation and photocurrent, the conversion efficiency of the near-field TPV system can be obtained as shown in Fig. 15(c). For comparison, the conversion efficiency for the ideal case with 100% quantum efficiency is also plotted. If the quantum efficiency is 100%, all photogenerated electron-hole pairs contribute to the power generation without being recombined during the diffusion to the depletion region. For such case, the conversion efficiency increases as the vacuum gap decreases and can reach as high as 35% when $d = 5$ nm. The conversion efficiency calculated by considering recombination is lower than the ideal case by 5% to 10%, and experiences a decrease as the vacuum gap further decreases below 10 nm. This efficiency decrease is due to the extremely small penetration depth of evanescent waves on the order of a nanometer: electron-hole pairs generated in proximity to the surface will be subject to more recombination while they move to the depletion region (Basu and Zhang, 2009b).

Figure 15 clearly shows that the near-field TPV can greatly enhance the power generation with approximately 20% conversion efficiency. The power density at the vacuum gap of 100 nm is predicted to be $\sim$20 W/cm$^2$, suggesting that about 65 cm$^2$ (or 8 cm $\times$ 8 cm) of a TPV cell could generate enough electric power that meets the demand of one US household, i.e., monthly average of 958 kWh in 2010 as reported by the US Energy Information Administration (http://www.eia.gov). However, it should be noted that this prediction is based on the semi-infinite tungsten emitter maintained at 2000 K, assumed as a reservoir, and thus energy required to maintain 2000 K was not taken into consideration. Another issue is that temperature increase of the TPV cell due to thermalization of high-energy charge carriers was not considered although it will adversely affect the performance of the TPV cell. Together with the promising results, these limiting factors strongly suggest the near-field effect on the TPV energy conversion should be experimentally and fundamentally investigated to validate the theoretical prediction of the device performance. However, it remains extremely challenging to design and fabricate a near-field TPV system, particularly in keeping a large area within a sub-100-nm vacuum gap with good parallelism. Although
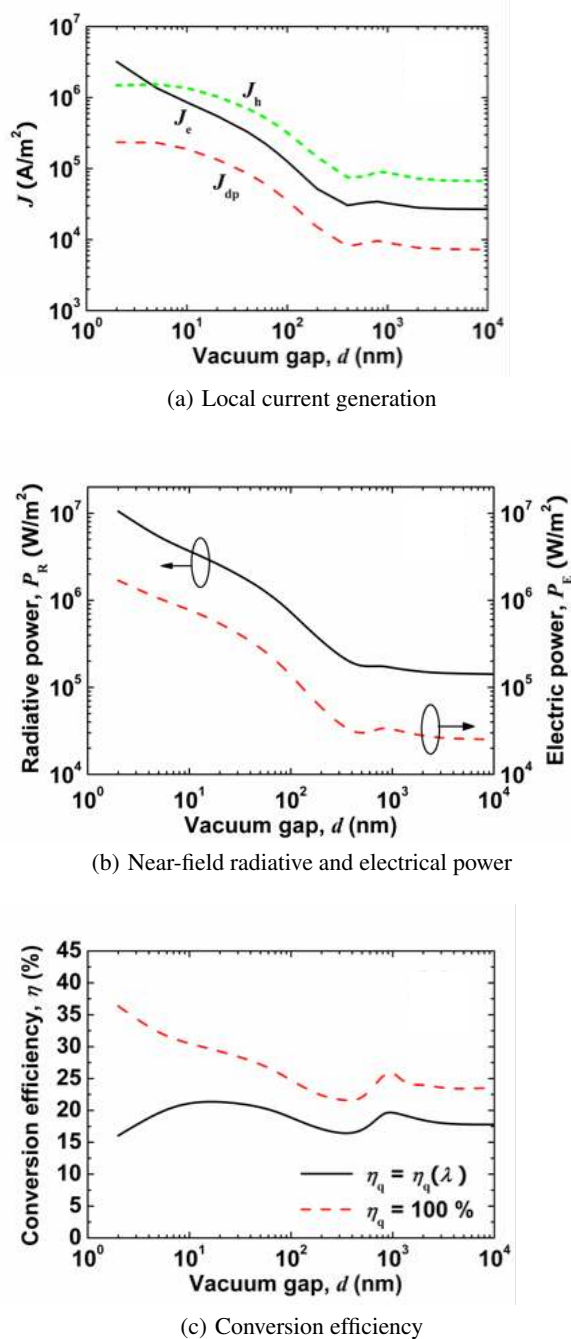
(a) Local current generation



(b) Near-field radiative and electrical power



(c) Conversion efficiency

**Fig. 15** The effect of vacuum gap width $d$ on (a) the local current generation, (b) the absorbed radiative power and electrical power generation, and (c) the conversion efficiency. The conversion efficiency for $\eta_q = 100\,\%$ is also plotted for comparison (Park et al., 2008).

near-field radiation has been experimentally verified, as discussed in the previous section, only near-field thermal radiation between a sphere and flat substrate has been measured near room temperature (Kittel et al., 2005; Narayanaswamy et al., 2008; Shen et al., 2009, 2012; Rousseau et al., 2009). Nanoscale thermal radiation between two flat surfaces has not been experimentally demonstrated despite several attempts in the past (Domoto et al., 1969; Hargreaves, 1969; Xu et al., 1994). Considering that the sphere-to-substrate case is not the adequate geometry for a near-field TPV system, parallelism between two flat surfaces with a small gap distance must be realized for the development of the near-field

TPV system. Recently, Ottens et al. (2011) demonstrated near-field effect on the radiative heat flux between flat sapphire plates separated at a distance as small as 1-2 $\mu$m. DiMatteo et al. (2003) suggested using tubular spacers between the emitter and TPV cell to realize a sub-micron vacuum gap and also to prevent parasitic conduction heat transfer between the thermal emitter and the TPV cell. Based on previous research results, their concept is in the phase of commercialization (http://www.mtpvcorp.com): the first generation module that generates the current density of 1 W/cm$^2$ has been developed, being anticipated to advance it to 40 - 50 W/cm$^2$ within two years.

### 6.3. Tip-Based Applications Using Near-Field Thermal Radiation

Highly enhanced near-field thermal radiation between a tip and substrate has been used to develop novel scanning probe microscopies and spectroscopies. De Wilde et al. (2006) has developed thermal radiation scanning tunneling microscopy (TRSTM), which is a scattering-type near-field scanning optical microscopy (NSOM) in the infrared spectrum (Tersoff and Hamann, 1985), but without any external illumination. When a gold-coated tip scans over a heated SiC samples with gold patterns, thermally excited surface waves in the infrared, i.e., SPPs on gold and SPhPs on SiC, are near-field interacted and scattered by the tip. By measuring the scattered thermal emission with a HgCdTe detector, they could achieve the near-field image of the sample along with the AFM topographic image. In fact, TRSTM can measure the electromagnetic local density of states (LDOS) at a frequency that can be defined by a suitable filter: this is analogous to the scanning tunneling microscopy that probes the electronic LDOS (Tersoff and Hamann, 1985). Recently, Jones and Raschke (2012) reported another exciting tip-based metrology utilizing near-field thermal radiation. By combining scattering-type NSOM with Fourier-transform spectroscopy and using a heated atomic force microscope tip as both a local thermal source and scattering probe, they obtained the mid-infrared spectrum of thermal near-field scattered from the tip with the spatial resolution of ~50 nm. The developed thermal infrared near-field optical spectroscopy can measure a highly localized spectral near-field energy density change associated with vibrational, phonon, and phonon-polariton modes of a substrate, enabling broadband chemical nanospectroscopy without the need for an external excitation source.

In addition to nanoimaging and nanospectroscopy instrumentations, tip-induced near-field radiation can be beneficially used for laser-based processing and structuring of materials at the nanoscale, in the order of ~50 nm or smaller. Upon illuminating a silicon tip or a metal-coated tip with a femtosecond laser, electromagnetic fields will be highly concentrated at the tip apex due to the optical antenna effect (Au et al., 2008; Schuller et al., 2009) and the excitation of localized surface polaritons (Chimmalgi et al., 2003; Milner et al., 2008). This EM field concentration may cause surface modification either through a hot tip interaction with a surface, leading to the melting/evaporation of the material (Kirsanov et al., 2003), or EM field enhancement under tip triggering the material ablation (Chimmalgi et al., 2003; Milner et al., 2008). When compared with other tip-based nanomanufacturing technologies, such as dip-pen nanolithography (e.g., Piner et al., 1999), thermal tip-based processing (e.g., Pires et al., 2010; Lee et al., 2010; Wei et al., 2010), and chemomechanical nanoscale patterning (e.g., Wacaser et al., 2003; Liu et al., 2004), the laser-based nanoscale material processing has a compelling advantage in manufacturable materials: its high energy concentration enables the nanoscale ablation and deposition of high melting-point metals, such as Au and FeCr (Chimmalgi et al., 2003; Kirsanov et al., 2003; Milner et al., 2008; Grigoropoulos et al., 2007). Moreover, the tip-induced scattering of laser beam could be collected to enable nanoscale optical imaging of the surface under fabrication, which will help the post-processing examination. Slow speed and low throughput still remain as challenging issues to be overcome for further advances of tip-based nanomanufacturing. However, various schemes are being proposed to operate multiple probes in parallel (Minne

*et al.*, 1998; Vettiger *et al.*, 2002) at high speeds (Ando, 2012), which will enhance throughput by more than two orders of magnitude.

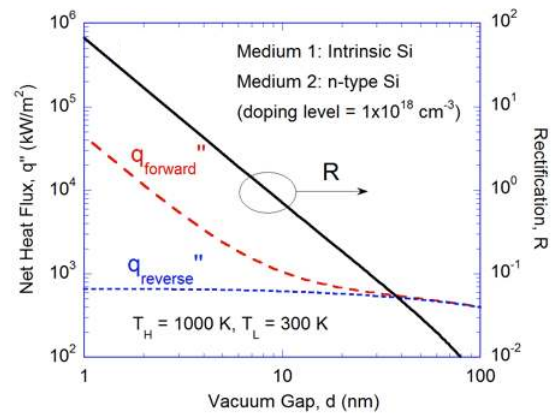### 6.4. Radiation-Based Thermal Rectification

Thermal rectification has recently attracted great attention since it could allow heat to flow in a preferred direction, and may have promising applications in thermal management and energy systems. Solid-state thermal rectifiers can be realized by asymmetric geometric or interface arrangements, dissimilar materials with different temperature-dependent thermal conductivity, and quantum structures (Stevenson *et al.*, 1990; Li *et al.*, 2004; Chang *et al.*, 2006; Dames, 2008; Hu *et al.*, 2009; Wu and Segal, 2009; Roberts and Walker, 2011). While most solid-state thermal rectifiers are based on the nonlinear phononic, electronic or mechanical properties of materials near the interfaces, a photonic device may be advantageous for obtaining large rectification factors over a broad temperature range. Near-field radiation has been theoretically demonstrated for potential application as thermal rectifiers between planar structures (Otey *et al.*, 2010; Iizuka and Fan, 2012; Basu and Francoeur, 2011a; Wang and Zhang, 2013). The basic concept is based on the different temperature dependences of the dielectric functions $\varepsilon_1$ and $\varepsilon_2$ of the two materials as shown in Fig. 1. The forward heat flux $q''_{\text{forward}} = q''_{12,\text{net}}$ refers to the situation when medium 1 is at a higher temperature $T_1 = T_H$ and medium 2 is at a lower temperature $T_2 = T_L$. The reverse-bias heat flux $q''_{\text{forward}} = q''_{21,\text{net}}$ refers to the situation when $T_1 = T_L < T_H = T_2$. Thermal rectification factor or simply thermal rectification is defined as (Dames, 2008; Wang and Zhang, 2013)

$$R = \frac{q''_{\text{forward}}}{q''_{\text{backward}}} - 1 \qquad (30)$$

which depends on the materialǎŹs choice as well as both $T_H$ and $T_L$.

Otey *et al.* (2010) theoretically obtained a rectification factor $R = 0.41$ by considering two SiC plates of different phases, an isotropic 3C-SiC plate and a uniaxial 6H-SiC plate, at $T_H = 600$ K and $T_L = 300$ K with a separation distance less than 100. The dielectric functions of SiC with different crystalline structures exhibit different temperature dependence, particularly due to the fact that the resonance frequencies of the two structures of SiC varies with temperature in opposite directions. This allows photon tunneling to be enhanced when the two resonance frequencies of SPhPs at each interface become closer. Iizuka and Fan (2012) studied the thermal rectification between coated and uncoated SiC plates, and optimized the permittivity and thickness of the coating to achieve a maximal rectification factor of 0.44 when the high and low temperatures are 500 K and 300 K, respectively. Basu and Francoeur (2011a) considered a thin Si film and a semi-infinite Si medium with different doping levels and obtained R = 0.51 at $d = 10$ nm with only 100 K temperature difference between the two media. Photon-mediated thermal rectifiers may be applicable to a large temperature range.

Wang and Zhang (2013) investigate the thermal rectification effect enabled by near-field radiative heat transfer between intrinsic silicon and several dissimilar materials including doped Si, SiO$_2$, and Au. The temperature-dependent properties of doped Si were taken from (Fu and Zhang, 2006). For Au, the Drude model was used and scattering rate is treated as proportional to temperature due to electron-phonon scattering. At elevated temperatures, free-carrier absorption becomes important in intrinsic Si due to the thermally excited charge carriers. When the intrinsic Si is at a temperature of $T_H = 1000$ K and the doped Si is at a temperature of $T_L = 300$ K, the dielectric functions of both media are dominated by free carriers, resulting in greatly enhanced heat flux, particularly as the vacuum gap is at the nanoscales. In the reverse-bias scenario, the intrinsic Si at 300 K behaves like a non-absorbing medium at wavelengths longer than 1.1 $\mu$m, except for some weak phonon absorptions. As shown in Fig. 16(a), the reverse heat flux is much lower at nanometer scales. Rectification factors $R = 0.71$, 2.7, and 67 were predicted at $d = 10$, 5, and 1 nm. The strong enhanced near-field



(a) Intrinsic Si vs. heavily doped Si
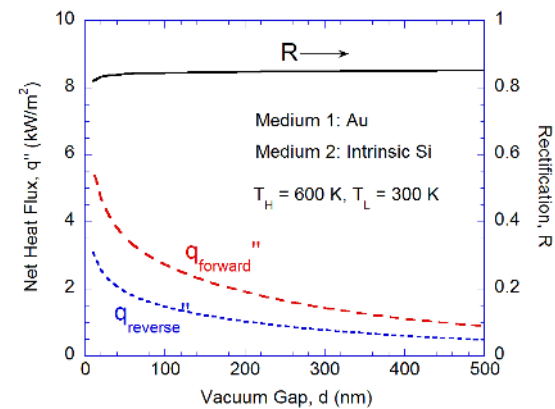


(b) Vacuum gap dependence (Au - intrinsic Si)
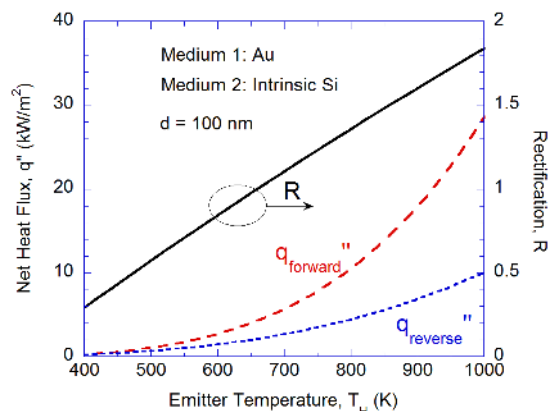


(c) $T_H$ dependence (Au - intrinsic Si)

**Fig. 16** Heat fluxes and thermal rectification between different materials (Wang and Zhang, 2013). (a) intrinsic Si versus heavily doped Si (n-type with a doping concentration of $10^{18}$ cm$^3$) at temperatures of $T_H = 1000$ K and $T_L = 300$ K. (b) Au (as medium 1) and intrinsic Si (as medium 2) at $T_H = 600$ K and $T_L = 300$ K for varying vacuum gap $d$. (c) Au versus intrinsic Si at $d = 100$ nm and $T_L = 300$ K for varying $T_H$.

radiation for forward bias is attributed to coupled SPPs (Wang and Zhang, 2013; Basu *et al.*, 2010b).

The calculated heat fluxes and rectification between Au and the intrinsic Si are shown in Fig. 16(b) with $T_H = 600$ K and $T_L = 300$ K. Since the emitter temperature is much lower (600 K compared to 1000

K) and the coupling of non-resonant evanescent waves between Au and intrinsic Si is weaker, the heat fluxes are several orders lower than that between intrinsic Si and doped Si. Interestingly, the rectification factor $R$ between Au and intrinsic Si is nearly the same for 10 nm $< d <$ 500 nm, between 0.82 and 0.85. As the emitter temperature $T_{\mathrm{H}}$ increases, as shown in Fig. 16(c) for $d = 100$ nm, the rectification factor can be further enhanced, e.g., $R = 1.84$ for $T_{\mathrm{H}} = 1000$ K, indicating almost twice as much heat can be transferred from Au (1000 K) to intrinsic Si (300 K) than vice versa. The thermal rectification between Au and intrinsic Si may facilitate thermal management and heat control at intermediate temperatures with relatively large vacuum gaps.

## 7. SUMMARY AND OUTLOOK

This article reviews recent achievements of near-field radiative heat transfer research from fundamental to application perspectives. Contrary to far-field thermal radiation carried by propagating EM waves, radiative heat transfer in the near field is dominated by evanescent EM waves (or surface waves) and photon tunneling. Based on the flucutational electrodynamics, the contributions of such near-field phenomena to thermal radiation are discussed for semi-infinite planar structures. Near-field thermal radiation is influenced by the vacuum gap and radiative properties of materials. For example, when doped Si plates are placed in proximity, the free carriers caused by dopants in Si give rise to fluctuating currents that result in significant augments in the net radiative energy flux. The excitation of surface polaritons plays a key role in the enhancement of near-field thermal radiation. In ideal but not realistic materials, the maximum near-field thermal radiation, would occur when surface polaritons were excited at all wavelengths within extremely small gap distances on the order of one nanometer. Surface waves are also responsible for the extremely small penetration depth and the laterally shifted energy flow of near-field thermal radiation between planar structures.

Besides the semi-infinite media, near-field radiative heat transfer between various geometrics has been theoretically investigated. Mathematical and computational challenges in solving stochastic Maxwell's equations for objects with arbitrary geometries have been addressed by implementing certain approximations, such as dipole, multipole, and proximity approximations, or by applying the molecular dynamics numerical scheme. Various geometrical configurations, including sphere-sphere, sphere-plane, cylinder-cylinder, and cylinder-plane cases have been investigated to reveal the geometry-dependence of near-field radiative transfer. However, there are discrepancies in the obtained gap dependence of near-field thermal radiation between different numerical schemes; this is an issue that demands further research. Near-field radiative heat transfer in emerging materials, such as graphenes, photonic crystals, and negative-index metamaterials, has become a very interesting research topic. It has been theoretically shown that unique radiative properties of such materials, e.g., the tunability of surface polariton excitation frequencies in graphenes, the photonic band gap in photonic crystals, and the negative refractive index in metamaterials, could further enhance near-field thermal radiation.

Despite significant progress in the theory of near-field thermal radiation, quantitative measurements have remained a challenge at nanometer distances. During the past few years, some meaningful measurements have been made in the sphere-plane configuration to validate the theoretical predictions. However, measuring near-field heat transfer between two flat surfaces at the nanometer distances is extremely challenging due to surface roughness and nonparallelism of the plates. Several suggestions have been made to achieve good parallelism between two planar surfaces by placing micro/nanospacers between plates or by feedback-controlling the emitter position, but experiments were successful only in the micrometer range. Since the experimental investigation on near-field thermal radiation between flat plates is crucial for the development of near-field TPV devices, innovative approaches that can overcome these

barriers need to be designed and developed. Experimental investigations using emerging materials have not been scrutinized yet, although the material selection is critically important for manipulating near-field thermal radiation.

Among many potential applications utilizing near-field thermal radiation, including the manipulation of the radiative properties, nanoscale imaging and analysis, and thermal rectification, near-field TPV holds great promise as a novel renewable energy harvesting technology. Theoretical studies have revealed that the power throughput of the near-field TPV can be enhanced by 1-2 orders of magnitude due to near-field effects with approximately 20 % conversion efficiency. However, there remain issues that must be addressed. The cost of TPV systems should be reduced by developing inexpensive alloys for TPV cells and achieving a cost-effective vacuum sealing with good parallelism. Effective cooling systems need to be developed in order to prevent overheating of the TPV cells. Efforts are also needed to recycle the unusable photons back to the emitter. More importantly, a second-law thermodynamic analysis of TPV systems is required in order to establish the fundamental achievable efficiencies to guide future TPV development. Since the radiation entropy in the near-field regime has not been clarified yet, a satisfactory thermodynamic second-law interpretation of near-field thermal radiation does not exist. Non-equilibrium entropy needs to be employed to develop thermodynamic relations for near-field radiation and to provide a second-law analysis of photon tunneling and surface polariton phenomena.

Improvement in computational resources, ever-advancing micro/nanofabrication and nano-instrumentation techniques, and the unprecedented growth in materials science have created compelling opportunities in the fundamental research and applications of near-field radiative heat transfer. The field of nanoscale radiation keeps growing with excitement, providing a deeper understanding of the interplay among optical, thermal, mechanical, and electrical properties of materials at the nanoscale. The understanding of near-field interactions can also help design systems for far-field applications. The authors strongly believe that near-field thermal radiation will be beneficially used for novel applications in biological sensing, materials processing and manufacturing, and energy systems in the near future.

### NOMENCLATURE

| | |
|---|---|
| $c$ | speed of light in vacuum ($2.998 \times 10^8$ m s$^{-1}$) |
| $\mathbf{D}$ | electric displacement vector (C m$^{-2}$) |
| $d$ | vacuum gap distance (m) |
| $\mathbf{E}$ | electric field vector (V m$^{-1}$) |
| $\overline{\overline{\mathbf{G}}}$ | dyadic Green's function (m$^{-1}$) |
| $\mathbf{H}$ | magnetic field vector (A m$^{-1}$) |
| $h$ | heat transfer coefficient (W m$^{-2}$ K$^{-1}$) |
| $\hbar$ | Planck constant divided by $2\pi$ ($1.055 \times 10^{-34}$ J s) |
| $J$ | photocurrent density (A m$^{-2}$) |
| $\mathbf{j}$ | fluctuating current density (A m$^{-2}$) |
| $\mathbf{k}$ | wavevector (m$^{-1}$) |
| $k_{\mathrm{B}}$ | Boltzmann constant ($1.381 \times 10^{-23}$ J K$^{-1}$) |
| $N$ | doping concentration (cm$^{-3}$) |
| $n$ | refractive index |
| $q''$ | heat flux (W m$^{-2}$) |
| $R$ | radius (m) |
| $\mathbf{r}$ | vector in the radial direction (m) |
| $r$ | Fresnel reflection coefficient |
| $\mathbf{S}$ | spectral Poynting vector (W m$^{-2}$ s rad$^{-1}$) |
| $T$ | temperature (K) |
| $t$ | Fresnel transmission coefficient |

| | | |
|---|---|---|
| **x** | position vector (m) | |
| **z** | vector in the normal direction to surfaces (m) | |

*Greek Symbols*

| | |
|---|---|
| $\alpha$ | polarizability (m$^3$) |
| $\beta$ | parallel wavevector component (m$^{-1}$) |
| $\gamma$ | wavevector component in the $z$-direction (m$^{-1}$) |
| $\delta$ | penetration depth or skin depth (m) |
| $\varepsilon$ | relative permittivity (i.e., dielectric function) |
| $\varepsilon_0$ | electrical permittivity of vacuum ($8.854 \times 10^{-12}$ F m$^{-1}$) |
| $\eta$ | conversion efficiency |
| $\eta_q$ | quantum efficiency |
| $\Theta$ | mean energy of the Planck oscillator (J) |
| $\kappa$ | extinction coefficient |
| $\Lambda$ | period of a grating structure (m) |
| $\lambda$ | wavelength in vacuum (m) |
| $\mu$ | relative permeability |
| $\mu_0$ | magnetic permeability of vacuum ($4\pi \times 10^{-7}$ H m$^{-1}$) |
| $\sigma$ | Stefan-Boltzmann constant ($5.67 \times 10^{-8}$ W m$^{-2}$ K$^{-4}$) |
| $\sigma_0$ | dc electrical conductivity (S m$^{-1}$) |
| $\tau$ | relaxation time (s) |
| $\omega$ | angular frequency (rad s$^{-1}$) |

*Superscripts*

| | |
|---|---|
| p | $p$-polarization or TM wave |
| s | $s$-polarization or TE wave |

*Subscripts*

| | |
|---|---|
| 0,1,2 | medium index |
| dp | depletion region |
| e | electron |
| evan | evanescent wave |
| h | hole |
| m | magnetic |
| max | maximum |
| prop | propagating wave |
| $\lambda, \omega$ | spectral |

## REFERENCES

Ando, T., 2012, "High-Speed Atomic Force Microscopy Coming of Age," *Nanotechnology*, **23**(6), 062001.
http://dx.doi.org/10.1088/0957-4484/23/6/062001.

Au, Y.Y., Skulason, H.S., Ingvarsson, S., Klein, L.J., and Hamann, H.F., 2008, "Thermal radiation spectra of individual subwavelength microheaters," *Physical Review B*, **78**(8), 085402.
http://dx.doi.org/10.1103/PhysRevB.78.085402.

Basu, S., Chen, Y.B., and Zhang, Z.M., 2007, "Microscale Radiation in Thermophotovoltaic Devices - a Review," *International Journal of Energy Research*, **31**(6-7), 689–716.
http://dx.doi.org/10.1002/er.1286.

Basu, S., and Francoeur, M., 2011a, "Near-Field Radiative Transfer Based Thermal Rectification Using Doped Silicon," *Applied Physics Letters*, **98**(11), 113106.
http://dx.doi.org/10.1063/1.3567026.

Basu, S., and Francoeur, M., 2011b, "Penetration Depth in Near-Field Radiative Heat Transfer Between Metamaterials," *Applied Physics Letters*, **99**(14), 143107.
http://dx.doi.org/10.1063/1.3646466.

Basu, S., Lee, B.J., and Zhang, Z.M., 2010a, "Infrared Radiative Properties of Heavily Doped Silicon at Room Temperature," *Journal of Heat Transfer*, **132**(2), 023301.
http://dx.doi.org/10.1115/1.4000171.

Basu, S., Lee, B.J., and Zhang, Z.M., 2010b, "Near-Field Radiation Calculated with an Improved Dielectric Function Model for Doped Silicon," *Journal of Heat Transfer*, **132**(2), 023302.
http://dx.doi.org/10.1115/1.4000179.

Basu, S., Wang, L.P., and Zhang, Z.M., 2011, "Direct Calculation of Energy Streamlines in Near-Field Thermal Radiation," *Journal of Quantitative Spectroscopy and Radiative Transfer*, **112**(7), 1149–1155.
http://dx.doi.org/10.1016/j.jqsrt.2010.08.027.

Basu, S., and Zhang, Z.M., 2009a, "Maximum Energy Transfer in Near-Field Thermal Radiation at Nanometer Distances," *Journal of Applied Physics*, **105**(9), 093535.
http://dx.doi.org/10.1063/1.3125453.

Basu, S., and Zhang, Z.M., 2009b, "Ultrasmall Penetration Depth in Nanoscale Thermal Radiation," *Applied Physics Letters*, **95**(13), 133104.
http://dx.doi.org/10.1063/1.3238315.

Basu, S., Zhang, Z.M., and Fu, C.J., 2009, "Review of Near-Field Thermal Radiation and Its Application to Energy Conversion," *International Journal of Energy Research*, **33**(13), 1203–1232.
http://dx.doi.org/10.1002/er.1607.

Baxter, J., Bian, Z., Chen, G., Danielson, D., Dresselhaus, M.S., Fedorov, A.G., Fisher, T.S., Jones, C.W., Maginn, E., and Kortshagen, U., 2009, "Nanoscale Design to Enable the Revolution in Renewable Energy," *Energy & Environmental Science*, **2**(6), 559–588.
http://dx.doi.org/10.1039/b821698c.

Ben-Abdallah, P., Joulain, K., and Pryamikov, A., 2010, "Surface Bloch Waves Mediated Heat Transfer Between Two Photonic Crystals," *Applied Physics Letters*, **96**(14), 143117.
http://dx.doi.org/10.1063/1.3385156.

Biehs, S.A., Ben-Abdallah, P., Rosa, F.S.S., Joulain, K., and Greffet, J.J., 2011a, "Nanoscale Heat Flux Between Nanoporous Materials," *Optics Express*, **19**(S5), A1088–A1103.
http://dx.doi.org/10.1364/OE.19.0A1088.

Biehs, S.A., Rosa, F.S.S., and Ben-Abdallah, P., 2011b, "Modulation of Near-Field Heat Transfer Between Two Gratings," *Applied Physics Letters*, **98**(24), 243102.
http://dx.doi.org/10.1063/1.3596707.

Biehs, S.A., Tschikin, M., and Ben-Abdallah, P., 2012, "Hyperbolic Metamaterials as an Analog of a Blackbody in the Near Field," *Physical Review Letters*, **109**(10), 104301.
http://dx.doi.org/10.1103/PhysRevLett.109.104301.

Bimonte, G., Cappellin, L., Carugno, G., Ruoso, G., and Saadeh, D., 2009, "Polarized Thermal Emission by Thin Metal Wires," *New Journal of Physics*, **11**(3), 033014.
http://dx.doi.org/10.1088/1367-2630/11/3/033014.

Carrillo, L.Y., and Bayazitoglu, Y., 2011, "Nanorod near-field radiative heat exchange analysis," *Journal of Quantitative Spectroscopy and Radiative Transfer*, **112**(3), 412–419.
http://dx.doi.org/10.1016/j.jqsrt.2010.10.011.

Carrillo, L.Y., and Bayazitoglu, Y., 2012, "Sphere Approximation for Nanorod Near-Field Radiative Heat Exchange Analysis," *Nanoscale and Microscale Thermophysical Engineering*, **15**(3), 195–208.
http://dx.doi.org/10.1080/15567265.2011.597493.

Chang, C.W., Okawa, D., Majumdar, A., and Zettl, A., 2006, "Solid-State Thermal Rectifier," *Science*, **314**(5802), 1121–1124.
http://dx.doi.org/10.1126/science.1132898.

Chapuis, P.O., Laroche, M., Volz, S., and Greffet, J.J., 2008a, "Radiative heat transfer between metallic nanoparticles," *Applied Physics Letters*, **92**(20), 201906.
http://dx.doi.org/10.1016/j.physleta.2007.09.050.

Chapuis, P.O., Volz, S., Henkel, C., Joulain, K., and Greffet, J.J., 2008b, "Effects of Spatial Dispersion in Near-Field Radiative Heat Transfer Between Two Parallel Metallic Surfaces," *Physical Review B*, **77**(3), 035431.
http://dx.doi.org/10.1103/PhysRevB.77.035431.

Chen, G., 2006, "Nanoscale Heat Transfer and Nanostructured Thermoelectrics," *Components and Packaging Technologies, IEEE Transactions on*, **29**(2), 238–246.
http://dx.doi.org/10.1109/TCAPT.2006.875895.

Chen, Y.B., and Zhang, Z.M., 2007, "Design of Tungsten Complex Gratings for Thermophotovoltaic Radiators," *Optics communications*, **269**(2), 411–417.
http://dx.doi.org/10.1016/j.optcom.2006.08.040.

Chen, Y.B., and Zhang, Z.M., 2008, "Heavily Doped Silicon Complex Gratings as Wavelength-Selective Absorbing Surfaces," *Journal of Physics D: Applied Physics*, **41**(9), 095406.
http://dx.doi.org/10.1088/0022-3727/41/9/095406.

Chimmalgi, A., Choi, T.Y., Grigoropoulos, C.P., and Komvopoulos, K., 2003, "Femtosecond Laser Aperturless Near-Field Nanomachining of Metals Assisted by Scanning Probe Microscopy," *Applied Physics Letters*, **82**(8), 1146.
http://dx.doi.org/10.1063/1.1555693.

Cravalho, E.G., Tien, C.L., and Caren, R.P., 1966, "Effect of Small Spacings on Radiative Transfer Between Two Dielectrics," *Journal of Heat Transfer*, **89**(4), 351–358.
http://dx.doi.org/10.1115/1.3614396.

Cui, L., Huang, Y., and Wang, J., 2012, "Near-Field Radiative Heat Transfer Between Chiral Metamaterials," *Journal of Applied Physics*, **112**(8), 084309.
http://dx.doi.org/10.1063/1.4759055.

Dames, C., 2008, "Solid-State Thermal Rectification With Existing Bulk Materials," *Journal of Heat Transfer*, **131**(6), 061301.
http://dx.doi.org/10.1115/1.3089552.

De Wilde, Y., Formanek, F., Carminati, R., Gralak, B., Lemoine, P.A., Joulain, K., Mulet, J.P., Chen, Y., and Greffet, J.J., 2006, "Thermal Radiation Scanning Tunnelling Microscopy," *Nature*, **444**(7120), 740–743.
http://dx.doi.org/10.1038/nature05265.

Derjaguin, B.V., Abrikosova, I.I., and Lifshitz, E.M., 1956, "Direct Measurement of Molecular Attraction Between Solids Separated by a Narrow Gap," *Quarterly Reviews of the Chemical Society*, **10**(3), 295–329.
http://dx.doi.org/10.1039/QR9561000295.

Dillner, U., 2008, "The Effect of Thermotunneling on the Thermoelectric Figure of Merit," *Energy Conversion and Management*, **49**(12), 3409–3416.
http://dx.doi.org/10.1063/1.3238315.

DiMatteo, R.S., Greiff, P., Finberg, S.L., Young-Waithe, K.A., Choy, H.K.H., Masaki, M.M., and Fonstad, Jr., C.G., 2003, "Microngap ThermoPhotoVoltaics (MTPV)," *AIP Conference Proceedings*, **653**, 232–240.
http://dx.doi.org/10.1063/1.1539379.

Domingues, G., Volz, S., Joulain, K., and Greffet, J.J., 2005, "Heat Transfer Between Two Nanoparticles Through Near Field Interaction," *Physical Review Letters*, **94**, 085901.
http://dx.doi.org/10.1103/PhysRevLett.94.085901.

Domoto, G.A., Boehm, R.F., and Tien, C.L., 1969, "Experimental Investigation of Radiative Transfer Between Metallic Surfaces at Cryogenic Temperatures," *Journal of Heat Transfer*, **92**(3), 412–416.
http://dx.doi.org/10.1115/1.3449677.

Dorofeyev, I.A., 1998, "Energy dissipation rate of a sample-induced thermal fluctuating field in the tip of a probe microscope," *Journal of Physics D: Applied Physics*, **31**(6), 600.
http://dx.doi.org/10.1088/0022-3727/31/6/004.

Dorofeyev, I., 2008, "Rate of Heat Transfer Between a Probing Body and a Sample Due to Electromagnetic Fluctuations," *Physics Letters A*, **372**(9), 1341–1347.
http://dx.doi.org/10.1016/j.physleta.2007.09.050.

Fan, Y., Singer, S.B., Bergstrom, R., and Regan, B.C., 2009, "Probing Planck's Law with Incandescent Light Emission From a Single Carbon Nanotube," *Physical Review Letters*, **102**(18), 187402.
http://dx.doi.org/10.1103/PhysRevLett.102.187402.

Francoeur, M., Basu, S., and Petersen, S.J., 2011a, "Electric and Magnetic Surface Polariton Mediated Near-Field Radiative Heat Transfer Between Metamaterials Made of Silicon Carbide Particles," *Optics Express*, **19**(20), 18774–18788.
http://dx.doi.org/10.1364/OE.19.018774.

Francoeur, M., Mengüç, M.P., and Vaillon, R., 2008, "Near-Field Radiative Heat Transfer Enhancement via Surface Phonon Polaritons Coupling in Thin Films," *Applied Physics Letters*, **93**(4), 043109.
http://dx.doi.org/10.1063/1.2963195.

Francoeur, M., Mengüç, M.P., and Vaillon, R., 2009, "Solution of Near-Field Thermal Radiation in One-Dimensional Layered Media Using Dyadic Green's Functions and the Scattering Matrix Method," *Journal of Quantitative Spectroscopy and Radiative Transfer*, **110**(18), 2002–2018.
http://dx.doi.org/10.1016/j.jqsrt.2009.05.010.

Francoeur, M., Vaillon, R., and Mengüç, M.P., 2011b, "Thermal Impacts on the Performance of Nanoscale-Gap Thermophotovoltaic Power Generators," *IEEE Transactions on Energy Conversion*, **26**(2), 686–698.
http://dx.doi.org/10.1109/TEC.2011.2118212.

Frank, I.W., Tanenbaum, D.M., van der Zande, A.M., and McEuen, P.L., 2007, "Mechanical properties of suspended graphene sheets," *Journal of Vacuum Science & Technology B*, **25**(6), 2558–2561.
http://dx.doi.org/10.1116/1.2789446.

Freitag, M., Steiner, M., Martin, Y., Perebeinos, V., Chen, Z., Tsang, J.C., and Avouris, P., 2009, "Energy Dissipation in Graphene Field-Effect Transistors," *Nano Letters*, **9**(5), 1883–1888.
http://dx.doi.org/10.1021/nl803883h.

Fu, C.J., and Tan, W.C., 2009, "Near-Field Radiative Heat Transfer Between Two Plane Surfaces with One Having a Dielectric Coating," *Journal of Quantitative Spectroscopy and Radiative Transfer*, **110**(12), 1027–1036.
http://dx.doi.org/10.1016/j.jqsrt.2009.02.007.

Fu, C.J., and Zhang, Z.M., 2006, "Nanoscale Radiation Heat Transfer for Silicon at Different Doping Levels," *International Journal of Heat and Mass Transfer*, **49**(9–10), 1703–1718.
http://dx.doi.org/10.1016/j.ijheatmasstransfer.2005.09.037.

Fu, C.J., and Zhang, Z.M., 2009, "Thermal Radiative Properties of Metamaterials and Other Nanostructured Materials: a Review," *Frontiers of Energy and Power Engineering in China*, **3**(1), 11–26.
http://dx.doi.org/10.1007/s11708-009-0009-x.

Fu, C.J., Zhang, Z.M., and Tanner, D.B., 2005, "Planar Heterogeneous Structures for Coherent Emission of Radiation," *Optics Letters*, **30**(14), 1873–1875.
http://dx.doi.org/10.1364/OL.30.001873.

Geim, A.K., and Novoselov, K.S., 2007, "The rise of graphene," *Nature Materials*, **6**(3), 183–191.
http://dx.doi.org/10.1038/nmat1849.

Golyk, V.A., Krüger, M., and Kardar, M., 2012, "Heat Radiation From Long Cylindrical Objects," *Physical Review E*, **85**(4), 046603.
http://dx.doi.org/10.1103/PhysRevE.85.046603.

González-Cuevas, J.A., Refaat, T.F., Abedin, M.N., and Elsayed-Ali, H.E., 2006, "Modeling of the Temperature-Dependent Spectral Response of $In_{1-x}Ga_xSb$ Infrared Photodetectors," *Optical Engineering*, **45**(4), 044001.
http://dx.doi.org/10.1117/1.2192772.

Griffiths, D.J., 2012, *Introduction to Electrodynamics*, 4th ed., Addison Wesley.

Grigoropoulos, C.P., Hwang, D.J., and Chimmalgi, A., 2007, "Nanometer-Scale Laser Direct-Write Using Near-Field Optics," *MRS Bulletin*, **32**(1), 16–22.
http://dx.doi.org/10.1557/mrs2007.10.

Hargreaves, C.M., 1969, "Anomalous Radiative Transfer Between Closely-Spaced Bodies," *Physics Letters A*, **30A**(9), 491–492.
http://dx.doi.org/10.1016/0375-9601(69)90264-3.

Howell, J.R., Siegel, R., and Mengüç, M.P., 2010, *Thermal Radiation Heat Transfer*, 5th ed., CRC Press.

Hu, L., Narayanaswamy, A., Chen, X., and Chen, G., 2008, "Near-Field Thermal Radiation Between Two Closely Spaced Glass Plates Exceeding Planck's Blackbody Radiation Law," *Applied Physics Letters*, **92**(13), 133106.
http://dx.doi.org/10.1063/1.2905286.

Hu, M., Goicochea, J.V., Michel, B., and Poulikakos, D., 2009, "Thermal Rectification at Water/Functionalized Silica Interfaces," *Applied Physics Letters*, **95**(15), 151903.
http://dx.doi.org/10.1063/1.3247882.

Huth, O., Rüting, F., Biehs, S.A., and Holthaus, M., 2010, "Shape-Dependence of Near-Field Heat Transfer Between a Spheroidal Nanoparticle and a Flat Surface," *The European Physical Journal Applied Physics*, **50**(1), 10603.
http://dx.doi.org/10.1051/epjap/2010027.

Hutter, E., and Fendler, J.H., 2004, "Exploitation of Localized Surface Plasmon Resonance," *Advanced Materials*, **16**(19), 1685–1706.
http://dx.doi.org/10.1002/adma.200400271.

Iizuka, H., and Fan, S., 2012, "Rectification of Evanescent Heat Transfer Between Dielectric-Coated and Uncoated Silicon Carbide Plates," *Journal of Applied Physics*, **112**(2), 024304.
http://dx.doi.org/10.1063/1.4737465.

Ilic, O., Jablan, M., Joannopoulos, J.D., Celanovic, I., Buljan, H., and Soljačić, M., 2012a, "Near-Field Thermal Radiation Transfer Controlled by Plasmons in Graphene," *Physical Review B*, **85**(15), 155422.
http://dx.doi.org/10.1103/PhysRevB.85.155422.

Ilic, O., Jablan, M., Joannopoulos, J.D., Celanovic, I., and Soljačić, M., 2012b, "Overcoming the Black Body Limit in Plasmonic and Graphene Near-Field Thermophotovoltaic Systems," *Optics Express*, **20**(S3), A366–A384.
http://dx.doi.org/10.1364/OE.20.00A366.

Ingvarsson, S., Klein, L., Au, Y.Y., Lacey, J.A., and Hamann, H.F., 2007, "Enhanced thermal emission from individual antenna-like nanoheaters," *Optics Express*, **15**(18), 11249–11254.
http://dx.doi.org/10.1364/OE.15.011249.

John, S., 1987, "Strong Localization of Photons in Certain Disordered Dielectric Superlattices," *Physical Review Letters*, **58**(23), 2486–2489.
http://dx.doi.org/10.1103/PhysRevLett.58.2486.

Jones, A.C., and Raschke, M.B., 2012, "Thermal Infrared Near-Field Spectroscopy," *Nano Letters*, 120301010022003.
http://dx.doi.org/10.1021/nl204201g.

Joulain, K., 2008, "Near-Field Heat Transfer: a Radiative Interpretation of Thermal Conduction," *Journal of Quantitative Spectroscopy and Radiative Transfer*, **109**(2), 294–304.
http://dx.doi.org/10.1016/j.jqsrt.2007.08.028.

Joulain, K., Drevillon, J., and Ben-Abdallah, P., 2010, "Noncontact Heat Transfer Between Two Metamaterials," *Physical Review B*, **81**(16), 165119.
http://dx.doi.org/10.1103/PhysRevB.81.165119.

Joulain, K., Mulet, J.P., Marquier, F., Carminati, R., and Greffet, J.J., 2005, "Surface Electromagnetic Waves Thermally Excited: Radiative Heat Transfer, Coherence Properties and Casimir Forces Revisited in the Near Field," *Surface Science Reports*, **57**(3–4), 59–112.
http://dx.doi.org/10.1016/j.surfrep.2004.12.002.

Ju, L., Geng, B., Horng, J., Girit, C., Martin, M., Hao, Z., Bechtel, H.A., Liang, X., Zettl, A., Shen, Y.R., and Wang, F., 2011, "Graphene Plasmonics for Tunable Terahertz Metamaterials," *Nature Nanotechnology*, **6**(10), 630–634.
http://dx.doi.org/10.1038/nnano.2011.146.

Kirsanov, A., Kiselev, A., Stepanov, A., and Polushkin, N., 2003, "Femtosecond Laser-Induced Nanofabrication in the Near-Field of Atomic Force Microscope Tip," *Journal of Applied Physics*, **94**(10), 6822.
http://dx.doi.org/10.1063/1.1621722.

Kittel, A., Muller-Hirsch, W., Parisi, J., Biehs, S.A., Reddig, D., and Holthaus, M., 2005, "Near-Field Heat Transfer in a Scanning Thermal Microscope," *Physical Review Letters*, **95**(22), 224301.
http://dx.doi.org/10.1103/PhysRevLett.95.224301.

Krüger, M., Emig, T., and Kardar, M., 2011, "Nonequilibrium electromagnetic fluctuations: Heat transfer and interactions," *Physical Review Letters*, **106**(21), 210404.
http://dx.doi.org/10.1103/PhysRevLett.106.210404.

Laroche, M., Carminati, R., and Greffet, J.J., 2006, "Near-Field Thermophotovoltaic Energy Conversion," *Journal of Applied Physics*, **100**(6), 063704.
http://dx.doi.org/10.1063/1.2234560.

Lee, B.J., Chen, Y.B., and Zhang, Z.M., 2008a, "Surface Waves Between Metallic Films and Truncated Photonic Crystals Observed with Reflectance Spectroscopy," *Optics Letters*, **33**(3), 204–206. http://dx.doi.org/10.1364/OL.33.000204.

Lee, B.J., Chen, Y.B., and Zhang, Z.M., 2008b, "Transmission Enhancement Through Nanoscale Metallic Slit Arrays From the Visible to Mid-Infrared," *Journal of Computational and Theoretical Nanoscience*, **5**, 201–213. http://dx.doi.org/10.1166/jctn.2008.008.

Lee, B.J., Fu, C.J., and Zhang, Z.M., 2005, "Coherent Thermal Emission From One-Dimensional Photonic Crystals ," *Applied Physics Letters*, **87**(7), 071904. http://dx.doi.org/10.1063/1.2010613.

Lee, B.J., Park, K., and Zhang, Z.M., 2007, "Energy Pathways in Nanoscale Thermal Radiation," *Applied Physics Letters*, **91**(15), 153101. http://dx.doi.org/10.1063/1.2793688.

Lee, B.J., Wang, L.P., and Zhang, Z.M., 2008c, "Coherent Thermal Emission by Excitation of Magnetic Polaritons Between Periodic Strips and a Metallic Film," *Optics Express*, **16**(15), 11328–11336. http://dx.doi.org/10.1364/OE.16.011328.

Lee, B.J., and Zhang, Z.M., 2006a, "Coherent Thermal Emission From Modified Periodic Multilayer Structures," *Journal of Heat Transfer*, **129**(1), 17–26. http://dx.doi.org/10.1115/1.2401194.

Lee, B.J., and Zhang, Z.M., 2006b, "Design and Fabrication of Planar Multilayer Structures with Coherent Thermal Emission Characteristics ," *Journal of Applied Physics*, **100**(6), 063529. http://dx.doi.org/10.1063/1.2349472.

Lee, B.J., and Zhang, Z.M., 2008, "Lateral Shifts in Near-Field Thermal Radiation with Surface Phonon Polaritons," *Nanoscale and Microscale Thermophysical Engineering*, **12**(3), 238–250. http://dx.doi.org/10.1080/15567260802247505.

Lee, J.U., Yoon, D., Kim, H., Lee, S.W., and Cheong, H., 2011, "Thermal conductivity of suspended pristine graphene measured by Raman spectroscopy," *Physical Review B*, **83**(8), 081419. http://dx.doi.org/10.1103/PhysRevB.83.081419.

Lee, J.I., Jeong, Y.H., No, H.C., Hannebauer, R., and Yoo, S.K., 2009, "Size Effect of Nanometer Vacuum Gap Thermionic Power Conversion Device with CsI Coated Graphite Electrodes," *Applied Physics Letters*, **95**(22), 223107. http://dx.doi.org/10.1063/1.3266921.

Lee, W.K., Dai, Z., King, W.P., and Sheehan, P.E., 2010, "Maskless Nanoscale Writing of NanoparticleâĹŠPolymer Composites and Nanoparticle Assemblies using Thermal Nanoprobes," *Nano Letters*, **10**(1), 129–133. http://dx.doi.org/10.1021/nl9030456.

Li, B., Wang, L., and Casati, G., 2004, "Thermal Diode: Rectification of Heat Flux," *Physical Review Letters*, **93**(18), 184301. http://dx.doi.org/10.1103/PhysRevLett.93.184301.

Li, P., Jiang, K., Liu, M., Li, Q., Fan, S., and Sun, J., 2003, "Polarized Incandescent Light Emission From Carbon Nanotubes," *Applied Physics Letters*, **82**(11), 1763–1765. http://dx.doi.org/10.1063/1.1558900.

Lin, S.Y., Moreno, J., and Fleming, J.G., 2003, "Three-Dimensional Photonic-Crystal Emitter for Thermal Photovoltaic Power Generation," *Applied Physics Letters*, **83**(2), 380–382. http://dx.doi.org/10.1063/1.1592614.

Liu, H., Genov, D.A., Wu, D.M., Liu, Y.M., Steele, J.M., Sun, C., Zhu, S.N., and Zhang, X., 2006, "Magnetic Plasmon Propagation Along a Chain of Connected Subwavelength Resonators at Infrared Frequencies," *Physical Review Letters*, **97**(24), 243902. http://dx.doi.org/10.1103/PhysRevLett.97.243902.

Liu, H., Li, T., Wang, Q.J., Zhu, Z.H., Wang, S.M., Li, J.Q., Zhu, S.N., Zhu, Y.Y., and Zhang, X., 2009, "Extraordinary Optical Transmission Induced by Excitation of a Magnetic Plasmon Propagation Mode in a Diatomic Chain of Slit-Hole Resonators," *Physical Review B*, **79**(2), 024304. http://dx.doi.org/10.1103/PhysRevB.79.024304.

Liu, J.F., Von Ehr, J.R., Baur, C., Stallcup, R., Randall, J., and Bray, K., 2004, "Fabrication of High-Density Nanostructures with an Atomic Force Microscope," *Applied Physics Letters*, **84**(8), 1359–1361. http://dx.doi.org/10.1063/1.1647281.

Liu, Y., and Zhang, X., 2011, "Metamaterials: a New Frontier of Science and Technology," *Chemical Society Reviews*, **40**(5), 2494–2507. http://dx.doi.org/10.1039/C0CS00184H.

Liu, Z.W., Wei, Q.H., and Zhang, X., 2005, "Surface Plasmon Interference Nanolithography," *Nano Letters*, **5**(5), 957–961. http://dx.doi.org/10.1021/nl0506094.

McCauley, A.P., 2012, "Modeling near-field radiative heat transfer from sharp objects using a general three-dimensional numerical scattering technique," *Physical Review B*, **85**(16), 165104. http://dx.doi.org/10.1103/PhysRevB.85.165104.

Milner, A.A., Zhang, K., and Prior, Y., 2008, "Floating Tip Nanolithography," *Nano Letters*, **8**(7), 2017–2022. http://dx.doi.org/10.1021/nl801203c.

Minne, S.C., Yaralioglu, G., Manalis, S.R., Adams, J.D., Zesch, J., Atalar, A., and Quate, C.F., 1998, "Automated Parallel High-Speed Atomic Force Microscopy," *Applied Physics Letters*, **72**(18), 2340. http://dx.doi.org/10.1063/1.121353.

Modest, M.F., 2003, *Radiative Heat Transfer*, 2nd ed., Elsevier Science, San Diego.

Mulet, J.P., Joulain, K., Carminati, R., and Greffet, J.J., 2001, "Nanoscale Radiative Heat Transfer Between a Small Particle and a Plane Surface," *Applied Physics Letters*, **78**(19), 2931–2933. http://dx.doi.org/10.1063/1.1370118.

Mulet, J.P., Joulain, K., Carminati, R., and Greffet, J.J., 2002, "Enhanced Radiative Heat Transfer at Nanometric Distances," *Microscale Thermophysical Engineering*, **6**(3), 209–222. http://dx.doi.org/10.1080/10893950290053321.

Muller-Hirsch, W., Kraft, A., Hirsch, M.T., Parisi, J., and Kittel, A., 1999, "Heat Transfer in Ultrahigh Vacuum Scanning Thermal Microscopy," *Journal of Vacuum Science & Technology A*, **17**(4), 1205–1210. http://dx.doi.org/10.1116/1.581796.

Narayanaswamy, A., and Chen, G., 2003, "Surface Modes for Near Field Thermophotovoltaics," *Applied Physics Letters*, **82**(20), 3544–3546. http://dx.doi.org/10.1063/1.1575936.

Narayanaswamy, A., and Chen, G., 2004, "Thermal Emission Control with One-Dimensional Metallodielectric Photonic Crystals," *Physical Review B*, **70**(12).
http://dx.doi.org/10.1103/PhysRevB.70.125101.

Narayanaswamy, A., and Chen, G., 2005, "Thermal Radiation in 1D Photonic Crystals ," *Journal of Quantitative Spectroscopy and Radiative Transfer*, **93**(1–3), 175–183.
http://dx.doi.org/10.1016/j.jqsrt.2004.08.020.

Narayanaswamy, A., and Chen, G., 2008, "Thermal Near-Field Radiative Transfer Between Two Spheres," *Physical Review B*, **77**(7), 075125.
http://dx.doi.org/10.1103/PhysRevB.77.075125.

Narayanaswamy, A., Shen, S., and Chen, G., 2008, "Near-Field Radiative Heat Transfer Between a Sphere and a Substrate," *Physical Review B*, **78**(11), 115303.
http://dx.doi.org/10.1103/PhysRevB.78.115303.

Nelson, R.E., 2003, "A Brief History of Thermophotovoltaic Development," *Semiconductor Science and Technology*, **18**(5), S141–S143.
http://dx.doi.org/10.1088/0268-1242/18/5/301.

Novoselov, K.S., Geim, A.K., Morozov, S.V., Jiang, D., Katsnelson, M.I., Grigorieva, I.V., Dubonos, S.V., and Firsov, A.A., 2005, "Two-dimensional gas of massless Dirac fermions in graphene," *Nature*, **438**(7065), 197–200.
http://dx.doi.org/10.1038/nature04233.

Novoselov, K.S., Geim, A.K., Morozov, S.V., Jiang, D., Zhang, Y., Dubonos, S.V., Grigorieva, I.V., and Firsov, A.A., 2004, "Electric Field Effect in Atomically Thin Carbon Films," *Science*, **306**(5696), 666–669.
http://dx.doi.org/10.1126/science.1102896.

Öhman, Y., 1961, "Polarized Thermal Emission from Narrow Tungsten Filaments," *Nature*, **192**(4799), 254.
http://dx.doi.org/10.1038/192254a0.

O'Sullivan, F., Celanovic, I., Jovanovic, N., Kassakian, J., Akiyama, S., and Wada, K., 2005, "Optical Characteristics of One-Dimensional Si/SiO2 Photonic Crystals for Thermophotovoltaic Applications," *Journal of Applied Physics*, **97**(3), 033529.
http://dx.doi.org/10.1063/1.1849437.

Otey, C.R., Lau, W.T., and Fan, S., 2010, "Thermal Rectification Through Vacuum," *Physical Review Letters*, **104**(15), 154301.
http://dx.doi.org/10.1103/PhysRevLett.104.154301.

Ottens, R., Quetschke, V., Wise, S., Alemi, A.A., Lundock, R., Mueller, G., Reitze, D.H., Tanner, D.B., and Whiting, B.F., 2011, "Near-Field Radiative Heat Transfer Between Macroscopic Planar Surfaces," *Physical Review Letters*, **107**(1), 014301.
http://dx.doi.org/10.1103/PhysRevLett.107.014301.

Pan, J.L., Choy, H.K.H., and Fonstad, Jr., C.G., 2000, "Very Large Radiative Transfer Over Small Distances From a Black Body for Thermophotovoltaic Applications," *IEEE Transactions on Electron Devices*, **47**(1), 241–249.
http://dx.doi.org/10.1109/16.817591.

Park, K., Basu, S., King, W.P., and Zhang, Z.M., 2008, "Performance Analysis of Near-Field Thermophotovoltaic Devices Considering Absorption Distribution," *Journal of Quantitative Spectroscopy and Radiative Transfer*, **109**(2), 305–316.
http://dx.doi.org/10.1016/j.jqsrt.2007.08.022.

Park, K., Lee, B.J., Fu, C.J., and Zhang, Z.M., 2005, "Study of the Surface and Bulk Polaritons with a Negative Index Metamaterial," *Journal of the Optical Society of America B*, **22**(5), 1016–1023.
http://dx.doi.org/10.1364/JOSAB.22.001016.

Pendry, J.B., 1999, "Radiative Exchange of Heat Between Nanostructures," *Journal of Physics: Condensed Matter*, **11**(35), 6621–6633.
http://dx.doi.org/10.1088/0953-8984/11/35/301.

Pendry, J.B., 2000, "Negative Refraction Makes a Perfect Lens," *Physical Review Letters*, **85**(18), 3966–3969.
http://dx.doi.org/10.1103/PhysRevLett.85.3966.

Pérez-Madrid, A., Lapas, L.C., and Rubí, J.M., 2009, "Heat Exchange Between Two Interacting Nanoparticles Beyond the Fluctuation-Dissipation Regime," *Physical Review Letters*, **103**(4), 048301.
http://dx.doi.org/10.1103/PhysRevLett.103.048301.

Pérez-Madrid, A., Reguera, D., and Rubí, J.M., 2003, "Origin of the Violation of the Fluctuation–Dissipation Theorem in Systems with Activated Dynamics," *Physica A: Statistical Mechanics and its Applications*, **329**(3), 357–364.
http://dx.doi.org/10.1016/S0378-4371(03)00634-4.

Pérez-Madrid, A., Rubí, J.M., and Lapas, L.C., 2008, "Heat transfer between nanoparticles: Thermal conductance for near-field interactions," *Physical Review B*, **77**(15), 155417.
http://dx.doi.org/10.1103/PhysRevB.77.155417.

Persson, B.N.J., and Ueba, H., 2010a, "Heat Transfer Between Graphene and Amorphous SiO$_2$," *Journal of Physics: Condensed Matter*, **22**(46), 462201.
http://dx.doi.org/10.1088/0953-8984/22/46/462201.

Persson, B.N.J., and Ueba, H., 2010b, "Heat Transfer Between Weakly Coupled Systems: Graphene on a-SiO$_2$," *Europhysics Letters*, **91**(5), 56001.
http://dx.doi.org/10.1209/0295-5075/91/56001.

Piner, R., Zhu, J., Xu, F., Hong, S.H., and Mirkin, C.A., 1999, """ Dip-Pen" Nanolithography," *Science*, **283**(5402), 661–663.
http://dx.doi.org/10.1126/science.283.5402.661.

Pires, D., Hedrick, J.L., De Silva, A., Frommer, J., Gotsmann, B., Wolf, H., Despont, M., Duerig, U., and Knoll, A.W., 2010, "Nanoscale Three-Dimensional Patterning of Molecular Resists by Scanning Probes," *Science*, **328**(5979), 732–735.
http://dx.doi.org/10.1126/science.1187851.

Planck, M., 1914, *The Theory of Heat Radiation*, Blakiston's Son & Co, Philadelphia.

Pralle, M.U., Moelders, N., McNeal, M.P., Puscasu, I., Greenwald, A.C., Daly, J.T., Johnson, E.A., George, T., Choi, D.S., El-Kady, I., and Biswas, R., 2002, "Photonic Crystal Enhanced Narrow-Band Infrared Emitters," *Applied Physics Letters*, **81**(25), 4685–4687.
http://dx.doi.org/10.1063/1.1526919.

Raether, H., 1988, *Surface Plasmons on Smooth and Rough Surfaces and on Gratings*, Springer-Verlag, Berlin.

Roberts, N.A., and Walker, D.G., 2011, "A Review of Thermal Rectification Observations and Models in Solid Materials," *International Journal of Thermal Sciences*, **50**(5), 648–662.
http://dx.doi.org/10.1016/j.ijthermalsci.2010.12.004.

Rodriguez, A., Ilic, O., Bermel, P., Celanovic, I., Joannopoulos, J.D., Soljačić, M., and Johnson, S., 2011, "Frequency-Selective Near-Field Radiative Heat Transfer between Photonic Crystal Slabs: A Computational Approach for Arbitrary Geometries and Materials," *Physical Review Letters*, **107**(11), 114302.
http://dx.doi.org/10.1103/PhysRevLett.107.114302.

Rousseau, E., Siria, A., Jourdan, G., Volz, S., Comin, F., Chevrier, J., and Greffet, J.J., 2009, "Radiative Heat Transfer at the Nanoscale," *Nature Photonics*, **3**(9), 514–517.
http://dx.doi.org/10.1038/nphoton.2009.144.

Ruppin, R., 2000, "Surface Polaritons of a Left-Handed Medium," *Physics Letters A*, **277**(1), 61–64.
http://dx.doi.org/10.1016/S0375-9601(00)00694-0.

Ruppin, R., 2001, "Surface Polaritons of a Left-Handed Material Slab," *Journal of Physics: Condensed Matter*, **13**(9), 1811–1818.
http://dx.doi.org/10.1088/0953-8984/13/9/304.

Rytov, S.M., Kravtsov, Y.A., and Tatarskii, V.I., 1987, *Principles of Statistical Radiophysics*, vol. 3, Springer-Verlag, New York.

Sasihithlu, K., and Narayanaswamy, A., 2011, "Convergence of Vector Spherical Wave Expansion Method Applied to Near-Field Radiative Transfer," *Optics Express*, **19**(S4), A772–A785.
http://dx.doi.org/10.1364/OE.19.00A772.

Schuller, J.A., Taubner, T., and Brongersma, M.L., 2009, "Optical Antenna Thermal Emitters," *Nature Photonics*, **3**(11), 658–661.
http://dx.doi.org/10.1038/nphoton.2009.188.

Schwierz, F., 2010, "Graphene Transistors," *Nature Nanotechnology*, **5**(7), 487–496.
http://dx.doi.org/10.1038/nnano.2010.89.

Shelby, R.A., Smith, D.R., and Schultz, S., 2001, "Experimental Verification of a Negative Index of Refraction," *Science*, **292**(5514), 77–79.
http://dx.doi.org/10.1126/science.1058847.

Shen, S., Mavrokefalos, A., Sambegoro, P., and Chen, G., 2012, "Nanoscale Thermal Radiation Between Two Gold Surfaces," *Applied Physics Letters*, **100**(23), 233114.
http://dx.doi.org/10.1063/1.4723713.

Shen, S., Narayanaswamy, A., and Chen, G., 2009, "Surface Phonon Polaritons Mediated Energy Transfer Between Nanoscale Gaps," *Nano Letters*, **9**(8), 2909–2913.
http://dx.doi.org/10.1021/nl901208v.

Singer, S.B., Mecklenburg, M., White, E.R., and Regan, B.C., 2011, "Polarized Light Emission From Individual Incandescent Carbon Nanotubes," *Physical Review B*, **83**(23), 233404.
http://dx.doi.org/10.1103/PhysRevB.83.233404.

Smith, D.R., Schurig, D., and Pendry, J.B., 2002, "Negative Refraction of Modulated Electromagnetic Waves," *Applied Physics Letters*, **81**(15), 2713–2715.
http://dx.doi.org/10.1063/1.1512828.

Stevenson, P.F., Peterson, G.P., and Fletcher, L.S., 1990, "Thermal Rectification in Similar and Dissimilar Metal Contacts," *Journal of Heat Transfer*, **113**(1), 30–36.
http://dx.doi.org/10.1115/1.2910547.

Svetovoy, V., van Zwol, P., and Chevrier, J., 2012, "Plasmon Enhanced Near-Field Radiative Heat Transfer for Graphene Covered Dielectrics," *Physical Review B*, **85**(15), 155418.
http://dx.doi.org/10.1103/PhysRevB.85.155418.

Tersoff, J., and Hamann, D.R., 1985, "Theory of The Scanning Tunneling Microscope," *Physical Review B*, **31**(2), 805–813.
http://dx.doi.org/10.1103/PhysRevB.31.805.

Tsang, L., Kong, J.A., and Ding, K.H., 2004, *Scattering of Electromagnetic Waves, Theories and Applications*, Wiley, New York.

Tsang, L., Njoku, E., and Kong, J.A., 1974, "Microwave Thermal Emission From a Stratified Medium with Nonuniform Temperature Distribution," *Journal of Applied Physics*, **46**(12), 5127–5133.
http://dx.doi.org/10.1063/1.321571.

van Beest, B.W.H., Kramer, G.J., and van Santen, R.A., 1990, "Force Fields for Silicas and Aluminophosphates Based on Ab Initio Calculations," *Physical Review Letters*, **64**(16), 1955–1958.
http://dx.doi.org/10.1103/PhysRevLett.64.1955.

Vettiger, P., Cross, G., Despont, M., Drechsler, U., Dürig, U., Gotsmann, B., Haberle, W., Lantz, M.A., Rothuizen, H.E., Stutz, R., and Binnig, G.K., 2002, "The "Millipede" - Nanotechnology Entering Data Storage," *IEEE Transactions on Nanotechnology*, **1**(1), 39–55.
http://dx.doi.org/10.1109/TNANO.2002.1005425.

Volokitin, A.I., and Persson, B.N.J., 2001, "Radiative Heat Transfer Between Nanostructures," *Physical Review B*, **63**(20), 205404.
http://dx.doi.org/10.1103/PhysRevB.63.205404.

Volokitin, A.I., and Persson, B.N.J., 2004, "Resonant Photon Tunneling Enhancement of the Radiative Heat Transfer," *Physical Review B*, **69**(4), 045417.
http://dx.doi.org/10.1103/PhysRevB.69.045417.

Volokitin, A.I., and Persson, B.N.J., 2011, "Near-Field Radiative Heat Transfer Between Closely Spaced Graphene and Amorphous $SiO_2$," *Physical Review B*, **83**(24), 241407.
http://dx.doi.org/10.1103/PhysRevB.83.241407.

Wacaser, B.A., Maughan, M.J., Mowat, I.A., Niederhauser, T.L., Linford, M.R., and Davis, R.C., 2003, "Chemomechanical Surface Patterning and Functionalization of Silicon Surfaces Using an Atomic Force Microscope," *Applied Physics Letters*, **82**(5), 808–810.
http://dx.doi.org/10.1063/1.1535267.

Wang, L.P., and Zhang, Z.M., 2009, "Resonance Transmission or Absorption in Deep Gratings Explained by Magnetic Polaritons," *Applied Physics Letters*, **95**(11), 111904.
http://dx.doi.org/10.1063/1.3226661.

Wang, L.P., and Zhang, Z.M., 2011, "Phonon-Mediated Magnetic Polaritons in the Infrared Region," *Optics Express*, **19**(S2), A126–A135.
http://dx.doi.org/10.1364/OE.19.00A126.

Wang, L.P., and Zhang, Z.M., 2012, "Wavelength-Selective and Diffuse Emitter Enhanced by Magnetic Polaritons for Thermophotovoltaics," *Applied Physics Letters*, **100**(6), 063902.
http://dx.doi.org/10.1063/1.3684874.

Wang, L.P., and Zhang, Z.M., 2013, "Thermal Rectification Enabled by Near-field Radiative Heat Transfer Between Intrinsic Silicon and a Dissimilar Material," *Nanoscale and Microscale Thermophysical Engineering*, accepted for publication.

Wang, L., Uppuluri, S.M., Jin, E.X., and Xu, X., 2006, "Nanolithography Using High Transmission Nanoscale Bowtie Apertures," *Nano Letters*, **6**(3), 361–364.
http://dx.doi.org/10.1021/nl052371p.

Wang, X.J., Basu, S., and Zhang, Z.M., 2009, "Parametric Optimization of Dielectric Functions for Maximizing Nanoscale Radiative Transfer," *Journal of Physics D: Applied Physics*, **42**(24), 245403.
http://dx.doi.org/10.1088/0022-3727/42/24/245403.

Wei, Z., Wang, D., Kim, S., Kim, S.Y., Hu, Y., Yakes, M.K., Laracuente, A.R., Dai, Z., Marder, S.R., Berger, C., King, W.P., de Heer, W.A., Sheehan, P.E., and Riedo, E., 2010, "Nanoscale Tunable Reduction of Graphene Oxide for Graphene Electronics," *Science*, **328**(5984), 1373–1376.
http://dx.doi.org/10.1126/science.1188119.

Whale, M.D., and Cravalho, E.G., 2002, "Modeling and Performance of Microscale Thermophotovoltaic Energy Conversion Devices," *IEEE Transactions on Energy Conversion*, **17**(1), 130–142.
http://dx.doi.org/10.1109/60.986450.

Wu, L.A., and Segal, D., 2009, "Sufficient Conditions for Thermal Rectification in Hybrid Quantum Structures," *Physical Review Letters*, **102**(9), 095503.
http://dx.doi.org/10.1103/PhysRevLett.102.095503.

Xu, J.B., Lauger, K., Moller, R., Dransfeld, K., and Wilson, I.H., 1994, "Heat Transfer Between Two Metallic Surfaces at Small Distances," *Journal of Applied Physics*, **76**(11), 7209–7216.
http://dx.doi.org/10.1063/1.358001.

Yablonovitch, E., 1987, "Inhibited Spontaneous Emission in Solid-State Physics and Electronics," *Physical Review Letters*, **58**(20), 2059–2062.
http://dx.doi.org/10.1103/PhysRevLett.58.2059.

Zhang, Z.M., 2007, *Nano/Microscale Heat Transfer*, McGraw-Hill.

Zhang, Z.M., Fu, C.J., and Zhu, Q.Z., 2003, "Optical and Thermal Radiative Properties of Semiconductors Related to Micro/Nanotechnology," *Advances in Heat Transfer*, vol. 37, 179–296, Elsevier.
http://dx.doi.org/10.1016/S0065-2717(03)37003-0.

Zhang, Z.M., and Lee, B.J., 2006, "Lateral Shift in Photon Tunneling Studied by the Energy Streamline Method," *Optics Express*, **14**(21), 9963–9970.
http://dx.doi.org/10.1364/OE.14.009963.

Zhang, Z.M., and Wang, L.P., 2011, "Measurements and Modeling of the Spectral and Directional Radiative Properties of Micro/Nanostructured Materials," *International Journal of Thermophysics*, (available online).
http://dx.doi.org/10.1007/s10765-011-1036-5.

Zhang, Z.M., and Wang, X.J., 2012, "Unified Wien's Displacement Law in Terms of Logarithmic Frequency or Wavelength Scale," *Journal of Thermophysics and Heat Transfer*, **24**(1), 222–224.
http://dx.doi.org/10.2514/1.45992.

Zhang, Z., Park, K., and Lee, B.J., 2011, "Surface and Magnetic Polaritons on Two-Dimensional Nanoslab-Aligned Multilayer Structure," *Optics Express*, **19**(17), 16375–16389.
http://dx.doi.org/10.1364/OE.19.016375.

Zheng, Z., and Xuan, Y., 2011, "Theory of Near-Field Radiative Heat Transfer for Stratified Magnetic Media," *International Journal of Heat and Mass Transfer*, **54**(5-6), 1101–1110.
http://dx.doi.org/10.1016/j.ijheatmasstransfer.2010.11.012.

Zhu, Q., Lee, H.J., and Zhang, Z.M., 2009, "Radiative Properties of Materials with Surface Scattering or Volume Scattering: a Review," *Frontiers of Energy and Power Engineering in China*, **3**(1), 60–79.
http://dx.doi.org/10.1007/s11708-009-0011-3.